Hydrodynamic-driven morphogenesis of karst draperies: spatio-temporal analysis of the two-dimensional impulse response

Pier Giuseppe Ledda[1]†, Gioele Balestra[2], Gaétan Lerisson[1], Benoit Scheid[3], Matthieu Wyart[4] and François Gallaire[1]

[1]Laboratory of Fluid Mechanics and Instabilities, École Polytechnique Fédérale de Lausanne, Lausanne, CH-1015, Switzerland

[2]iPrint Institute, University of Applied Sciences and Arts of Western Switzerland, Fribourg, CH-1700, Switzerland

[3]TIPs, Université Libre de Bruxelles, Avenue F.D. Roosevelt 50, 1050 Bruxelles, Belgium

[4]Physics of Complex Systems Laboratory, École Polytechnique Fédérale de Lausanne, Lausanne, CH-1015, Switzerland,

(Received xx; revised xx; accepted xx)

We study the role of hydrodynamic instabilities in the morphogenesis of some typical karst draperies structures encountered in limestone caves. The problem is tackled using the long wave approximation for the fluid film that flows under an inclined substrate, in the presence of substrate variations that grow according to a deposition law. We numerically study the linear and non-linear evolution of a localized initial perturbation both in the fluid film and on the substrate, i.e. the Green function. A novel approach for the spatio-temporal analysis of two-dimensional signals resulting from linear simulations is introduced, based on the concepts of the Riesz transform and the monogenic signal, the multi-dimensional complex continuation of a real signal. This method allows for a deeper understanding of the pattern formation. The linear evolution of an initial localized perturbation in the presence of deposition is studied. The deposition linearly selects substrate structures aligned along the streamwise direction, as the spatio-temporal response is advected away. Furthermore, the growth of the initial defect produces a quasi-steady region also characterized by streamwise structures both on the substrate and the fluid film, which is in good agreement with the Green function for a steady defect on the substrate, in the absence of deposition.

1. Introduction

The astonishing beauty of geological patterns has fascinated humanity for centuries (Hill *et al.* 1997). Several different geological structures are related to mineral dissolution (Cohen *et al.* 2016) and precipitation (Meakin & Jamtveit 2010) in aqueous systems. A few examples are terraces and steps due to precipitation of dissolved minerals in flowing fluids on the ground, which find a parallel in the structures arising from melting and freezing of ice, usually called icicles and crenulations. Another class of geological patterns is speleothems, which are karst structures encountered in limestone caves. The most common structures are stalactites, stalagmites, draperies, flutings, to name a few. The chemical mechanism behind the growth of speleothems is the precipitation of calcium carbonate dissolved in water which flows on the cave walls. Due to the higher partial

† Email address for correspondence: pier.ledda@epfl.ch

pressure of CO_2 in the soil and rock compared to the atmosphere, flowing water enriches in carbon dioxide. The pH of the solution is lowered and the quantity of calcium carbonate that can be dissolved in water increases (Short *et al.* 2005*a*,*b*). Once the water enriched in CO_2 flows through an opening on the walls of a cave, the CO_2 outgases from the solution, the concentration in the air being lower than in the water. As a result, the solution is supersaturated and calcium carbonate minerals deposit on the surface (Buhmann & Dreybrodt 1985).

The role of hydrodynamics in the speleothem formation increased in interest in the last two decades. Short *et al.* (2005*a*) showed that the stalactite shape is self-similar and results from the coupling of hydrodynamics and the deposition process. In Camporeale & Ridolfi (2012) the problem of the origin of crenulations on stalactites was tackled in the context of falling film theory, indicating that the pattern is mainly dictated by a hydrodynamic instability (Vesipa *et al.* 2015). The emergence of draperies structures in limestone caves is also driven by falling liquid film instabilities (Bertagni & Camporeale 2017). Falling liquid films are usually described in the context of the long-wave or lubrication approximation (Kalliadasis *et al.* 2011), in which the fundamental assumption is that the interface modulation wavelengths are much larger than the characteristic thickness of the flowing film.

The dynamics of a viscous film underneath a substrate, and for which inertial effects are negligible, is related to the Rayleigh-Taylor instability. In the presence of gravitational forces, the flat interface is destabilized when a heavier fluid is placed above a lighter one (Rayleigh 1882; Taylor 1950). While gravity plays a destabilizing role, pushing the heavier fluid down, surface tension stabilizes disturbances of small wavelengths. In the case of a thin film coating the underside of a surface, the problem is solved in the context of the lubrication approximation (Babchin *et al.* 1983). When the substrate is horizontal, the resulting pattern is characterized by drops which organize in regular arrays (Fermigier *et al.* 1992) and can grow in time or saturate depending on the initial thickness (Lister *et al.* 2010; Marthelot *et al.* 2018).

If the substrate is inclined, there is a gravity component which is projected along the substrate, leading to a flow. The growth rate of perturbations decreases due to the reduction of the gravity component normal to the substrate, and perturbations can be advected away. A link between the absolute to convective transition of the flow instability and dripping was shown by Brun *et al.* (2015). A refined model including inertial and viscous extensional stresses for high flow rates demonstrated that the occurrence of the absolute instability does not predict the dripping satisfactorily (Scheid *et al.* 2016; Kofman *et al.* 2018). In Lerisson *et al.* (2020) and Ledda *et al.* (2020) the conditions for the existence of steady patterns and the selection mechanisms for a thin film flowing under an inclined planar substrate in the absence of inertial effects were experimentally and numerically studied. The flow can reach a steady state without dripping, characterized by elongated structures modulated along the direction perpendicular to the flow (*spanwise* direction), called rivulets, also observed experimentally in Charogiannis *et al.* (2018). It has been demonstrated that the rivulet profile reaches a state mainly driven by static arguments, i.e. a pure equilibrium between surface tension and capillary effects. A weakly non-linear model highlighted the selection mechanism of streamwise structures, and the stability analysis of the rivulet profile to streamwise perturbations revealed that short wavelengths are progressively stabilized as the substrate is more inclined or the liquid film thinner. Rivulets can therefore be a stable pattern, for certain values of angle, flow rate and streamwise length of the domain. Outside of this range, lenses appear on rivulets, and they may merge and eventually drip (Lerisson *et al.* 2019).

Bertagni & Camporeale (2017) studied the morphogenesis of draperies structures in

limestone caves using the thin film equation, combining a two-dimensional linear stability analysis and a weakly non-linear approach to show the emergence of streamwise structures (i.e. rivulets in the fluid film, draperies on the substrate, see fig. 1(a)). The growth rate of perturbations from a flat condition is slightly larger for streamwise aligned structures as the inertia of the flow is neglected. However, a complete characterization of the two-dimensional spatio-temporal dynamics and a description of the key mechanisms and the physics underlying the selection of streamwise structures on the substrate remain to be assessed. We will highlight in this work that a small coupling of the hydrodynamic effects with the deposition effect is already sufficient to induce a significant anisotropy in the spatio-temporal response, while it has only a minute effect in the temporal dispersion relation.

The response of a given flow to external perturbations can be characterized through the large-time asymptotic behavior of the linear impulse response, the Green function. The Green function is the most synthetic and complete way to describe the nature of a forced linear system, since the response to any generic forcing is given by the convolution between the Green function and the forcing itself. The impulse can be localized only in space (*steady* analysis) or both in space and time (*spatio-temporal* analysis). Considering the steady case, for a thin film flowing over an inclined planar substrate, the linear Green function enables the reconstruction of the response which emerges from the presence of localized defects (Kalliadasis *et al.* 2000; Hayes *et al.* 2000; Decré & Baret 2003). Interestingly, the resulting Green function for a steady defect is characterized by a decaying behavior as the distance from the defect location increases.

In unstable flows, the spatio-temporal Green function analysis is usually analytically tackled within the context of the *saddle points* approach, in which the large-time asymptotic properties of the response can be retrieved by the research of the saddle points of the spatio-temporal growth rate in the complex planes of the spatial wavenumbers which define the response (Briggs 1964; Bers 1975; Huerre & Monkewitz 1990; Carriere & Monkewitz 1999; Juniper 2007; Brun *et al.* 2015).

Alternatively, it has been demonstrated that a numerical approach based on the post-processing of the numerical linear impulse response can well describe the long-time behavior of the impulse response (Brancher & Chomaz 1997; Delbende *et al.* 1998; Delbende & Chomaz 1998; Gallaire & Chomaz 2003; Mowlavi *et al.* 2016; Lerisson 2017; Arratia *et al.* 2018). The procedure consists of a demodulation of the signal along one direction using the Hilbert transform, which leads to the complex analytic continuation of the real response, the analytic signal. As we detail in this study, the multi-dimensional counterpart of the analytic signal is the monogenic signal (Unser *et al.* 2009), which finds many applications in image analysis processes and is based on the application of the Riesz transform, the multi-dimensional generalization of the Hilbert transform.

In this work, we propose a numerical method for the analysis of the long-time asymptotic two-dimensional linear impulse response, with the aim of shedding light on the linear physical mechanisms which may lead to the selection of draperies structures on the substrate. The paper is organised as follows. In Section 2, the equations for the evolution of a thin film in the presence of substrate variations are defined. To introduce the numerical procedure for the analysis of the linear response in the presence of a deposition process, we first validate the algorithm against the results of the linear response in the absence of the deposition process and on a flat substrate, since in this circumstance the problem can be solved analytically. We define the theoretical framework of the linear impulse response and we derive the analytical solution for the thin film in the absence of substrate variations. We characterize the response, whose results will be used throughout the work as a comparison with the response in the presence of the deposition process.

(a) (b)

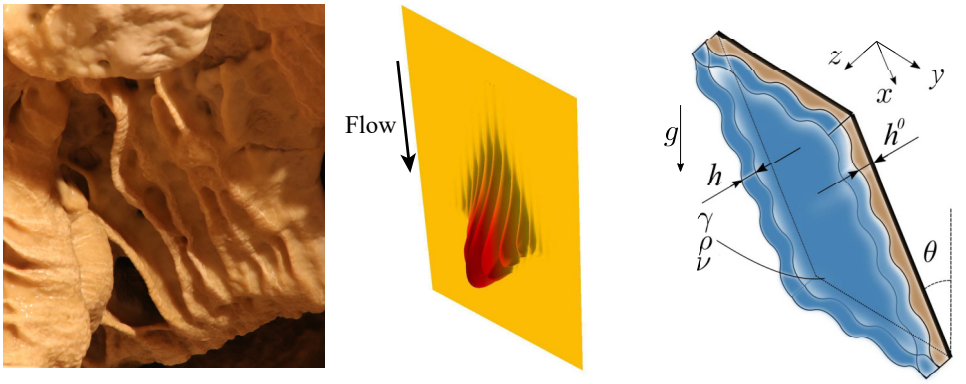

FIGURE 1. (a) Draperies observed in the Vallorbe caves, Switzerland (on the left), and sketch (on the right). (b) Description of the considered problem with the fluid film and substrate thickesses indicated.

Subsequently, in Section 4 we present the post-processing algorithm for the analysis of the spatio-temporal impulse response in two dimensions, which we validate using the theoretical results of the previous part. We exploit the validated numerical algorithm in Section 5, where we focus on the linear impulse response of a thin film in the presence of a deposition process. The numerical solution of the linearized flow equations is analyzed through the post-processing algorithm. An additional analytical tool for the validation and interpretation of the results is given in Section 6, focused on the study of the response in the presence of a steady defect without deposition processes. We compare the numerical results with an analytical approach for the evaluation of the steady Green function within the framework of spatial stability analysis. To verify the faithfulness of the results of the performed linear analyses, non-linear simulations in the presence of the deposition process are reported in Section 7.

2. Thin film model

We study the dynamics of a thin film of a viscous fluid flowing under a plane inclined with respect to the vertical of an angle θ, in the presence of substrate variations (fig. 1(b)). The fluid properties are the kinematic viscosity ν, the density ρ and the surface tension coefficient γ. We denote respectively the fluid film thickness and substrate variation thickness as $\bar{h}$ and $\bar{h}^0$. Thus, the distance of the fluid interface from the reference flat substrate is $\bar{h}+\bar{h}^0$. A coordinate system $(\bar{x},\bar{y})$ is defined, where $\bar{x}$ and $\bar{y}$ are respectively the streamwise and spanwise directions. We introduce the initial flat film (Nusselt) thickness h_N and the reduced capillary length l_c^*:

$$l_c^* = \frac{l_c}{\sqrt{\sin(\theta)}}, \tag{2.1}$$

where $l_c = \sqrt{\gamma/(\rho g)}$ is the capillary length. The following adimensionalizations are defined:

$$x = \bar{x}/l_c^*; \;\; y = \bar{y}/l_c^*; \;\; h = \bar{h}/h_N; \;\; t = \bar{t}/\tau_{\mathrm{RT}}, \tag{2.2}$$

where $\tau_{\mathrm{RT}} = \nu l_c^2/h_N^3 \sin^2(\theta) g$ is the characteristic time scale of the Rayleigh-Taylor instability.

The problem of the lubrication model in the presence of substrate variations has been widely studied in the literature, in the context of the long wave approximation (Tseluiko *et al.* 2013) or more involved models based on the introduction of inertia and viscous extensional effects (D'Alessio *et al.* 2010; Heining & Aksel 2009). In this work, we consider the model used in Bertagni & Camporeale (2017), for the inertialess case, in which the complete curvature is retained (Weinstein & Ruschak 2004; Wilson 1982). The adimensional equation for the evolution of the thickness in the presence of substrate variations reads:

$$\partial_t h + u h^2 \partial_x h + \frac{1}{3}\nabla \cdot \left[\chi h^3 \nabla(h + h^0) + h^3 \nabla \kappa\right] = 0, \tag{2.3}$$

where ∇ operates in the (x, y) plane and $u = \cot(\theta) l_c^*/h_N$ is the linear advection velocity (Brun *et al.* 2015). The constant χ is set to $\chi = 1$ for the flow under an inclined substrate, which is analyzed throughout the work, except in the Appendix A, where we report the validation of the numerical procedure against a benchmark case in the literature for the flow over an inclined flat substrate ($\chi = -1$). The curvature of the free surface is denoted as $\kappa = -\nabla \cdot \mathbf{n}$, where:

$$\mathbf{n} = \frac{[-\partial_x h - \partial_x h^0, -\partial_y h - \partial_y h^0, 1]^T}{\sqrt{1 + (\partial_x h^0 + \partial_x h)^2 + (\partial_y h^0 + \partial_y h)^2}} \tag{2.4}$$

is the normal to the free surface.

In this paper, we focus on the substrate growth by precipitation of calcium carbonate in cave walls. The mathematical formulation of the problem involves different chemical reactions and diffusion processes that occur in the fluid layer (Buhmann & Dreybrodt 1985). Following the derivation of Short *et al.* (2005*b*), to which we refer for details, the flux of calcium carbonate depositing on the substrate, i.e. the variation in time of the substrate thickness, can be written as follows:

$$\partial_{\bar{t}} \bar{h}^0 = \bar{C} \bar{h}, \tag{2.5}$$

where $\bar{C}$ is the chemistry-dependent constant, of the order of $\bar{C} \sim 10^{-7} s^{-1}$ (Camporeale 2015). Considering the time scale τ_{RT}, the deposition constant in the dimensionless time scale is of the order $C \sim 10^{-4}$. Introducing the adimensionalization eq. (2.2), the nondimensional equation for the deposition reads:

$$\partial_t h^0 = \check{C} h, \tag{2.6}$$

where $\check{C} = C/\sin^2(\theta)$. Equations (2.3) and (2.6) define the system for the dynamics of a thin film flowing under ($\chi = 1$) an inclined plane in the presence of substrate variations due to the deposition of calcium carbonate.

The equations are linearized around the baseflow solution $[H, H^0]^T = [1, \check{C}t]^T$ introducing the following decomposition:

$$h = 1 + \varepsilon\eta, \quad h^0 = \check{C}t + \varepsilon\eta^0, \tag{2.7}$$

where $\varepsilon \ll 1$ and $[\eta, \eta^0]$ is the *perturbation* with respect to the baseflow solution. Keeping $O(\varepsilon)$ terms in equations (2.3), (2.6), the following system of equations is obtained:

$$\partial_t \eta + u \partial_x \eta + \frac{1}{3}\left[\chi \nabla^2(\eta + \eta^0) + \nabla^4(\eta + \eta^0)\right] = 0, \tag{2.8a}$$

$$\partial_t \eta^0 = \check{C}\eta, \tag{2.8b}$$

(a) (b)

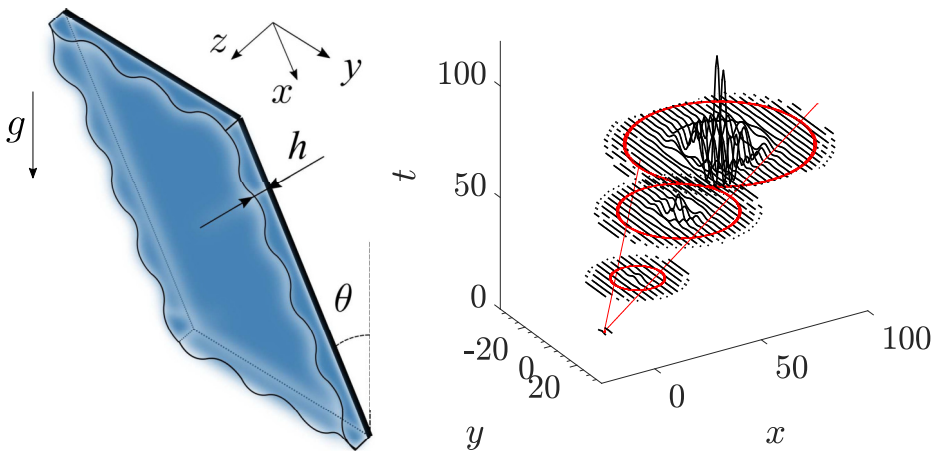

FIGURE 2. (a) Sketch of the flow and substrate configurations adopted in Section 3. (b) Sketch of the impulse reponse in a spatio-temporal diagram.

which describes the linearized dynamics of the *perturbation* $[\eta, \eta^0]$ around the constant flat film solution $H = 1$ (eq. 2.8a), in the presence of a linear in time substrate growth H^0 due to the deposition law (eq. 2.8b), i.e. $[H, H^0]^T = [1, \check{C}t]^T$. Equations (2.8) are the starting point for the analysis of the speleothems morphogenesis, in a linearized dynamics context.

The numerical implementation of the linearized equations (2.8) is based on a Fourier pseudo-spectral scheme implemented in MATLAB. Henceforth, we consider a rectangular domain of size 1000×1000, with a number of collocation points $N_x = N_y = 1001$ and periodic boundary conditions. In Appendix A we report the numerical procedure and the validation against the benchmark case of the response of a thin film flowing over an inclined flat substrate to a steady localized defect (Decré & Baret 2003; Kalliadasis *et al.* 2000; Hayes *et al.* 2000).

3. Linear response in the absence of substrate variations

3.1. *Dispersion relation*

In this section, we study the linear response in the absence of substrate variations (fig. 2). We therefore impose $\eta^0 = 0$ in eq. (2.8a), leading to the following equation for the linearized dynamics of the perturbation:

$$\partial_t \eta + u \partial_x \eta + \frac{1}{3}\left[\nabla^2 \eta + \nabla^4 \eta\right] = 0. \tag{3.1}$$

We introduce the ansatz $\eta \sim \exp[\mathrm{i}\,(k_x x + k_y y - \omega t)]$, where k_x and k_y are real and ω is complex, within the temporal approach. Introducing $k = \sqrt{k_x^2 + k_y^2}$, the following polynomial dispersion relation is obtained:

$$\omega = u k_x + \frac{\mathrm{i}}{3}\Big(k^2 - k^4\Big), \tag{3.2}$$

which relates the behavior in space and time of the perturbation. In the absence of deposition process, the temporal growth rate $\mathrm{Im}(\omega)$ does not depend on u, which

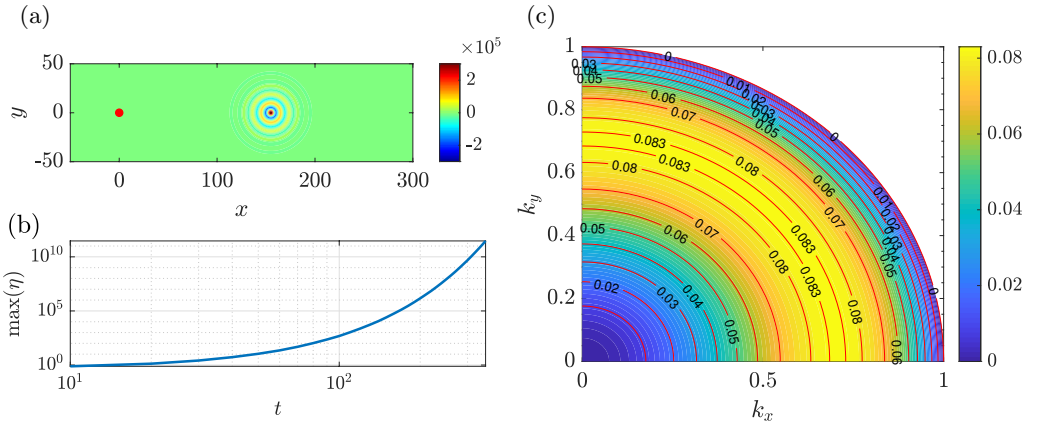

FIGURE 3. Two-dimensional linear impulse response in the absence of substrate variations, for $u = 0.77$. (a) Response in the physical space at $t = 200$. (b) Temporal evolution of the maximum value of the response. (c) Temporal growth rate, as a function of k_x and k_y. The red dot denotes the initial impulse location.

influences only the advection of perturbations. The response in the absence of deposition is characterized by concentric circles (see fig. 3(a)) that propagate from a center that is advected away with the linear advection velocity u. The maximum value of the thickness increases exponentially with time (see fig. 3(b)). In the following, we rescale the fluid thickness using the maximum value, knowing that the growth in amplitude is exponential. The iso-values of the temporal growth rate are concentric circles propagating from $(k_x, k_y) = 0$, (see fig. 3(c)), i.e. the growth rate is isotropic. The growth rate increases for small wavenumbers, reaches a maximum at $k = 1/\sqrt{2}$, then decreases and becomes negative for $k > 1$, the cut-off wavenumber. Therefore, the linearized dynamics does not show any preferential direction for the growth of perturbations, which are advected away.

3.2. *Large time behavior of the impulse response*

In this section, we analytically study the linear impulse large-time response. So as to better characterize the response observed in fig. 3(a) and understand the structure when the deposition process will be introduced, together with the differences with the case in the absence of substrate variations, we present the theoretical tools to describe the impulse response of a linear system, the Green function $\tilde{g}$. The method is a generalization of the classical one-dimensional approach (Brevdo 1991; Carriere & Monkewitz 1999; Juniper 2007). For $t \to \infty$, the Green function asymptotically reads:

$$\tilde{g}(x, y, t) \sim \hat{g} \exp[\mathrm{i}\,(k_x x + k_y y - \omega t)]/t, \quad t \to \infty \tag{3.3}$$

where the streamwise wavenumber k_x, the spanwise wavenumber k_y and the complex frequency ω are varying in space and time, via their dependence on so called rays x/t and y/t. The evaluation of the asymptotic properties along the rays ($x/t = \text{const}, y/t = \text{const}$) for $t \to \infty$ is performed using the method of the steepest descent in the complex k_x and k_y planes. At large times, the dominating contribution with group velocity $(x/t, y/t)$ is given by the following saddle points in the complex k_x and k_y planes:

$$\frac{\partial \omega''}{\partial k_x} = \frac{\partial \omega''}{\partial k_y} = 0, \tag{3.4}$$

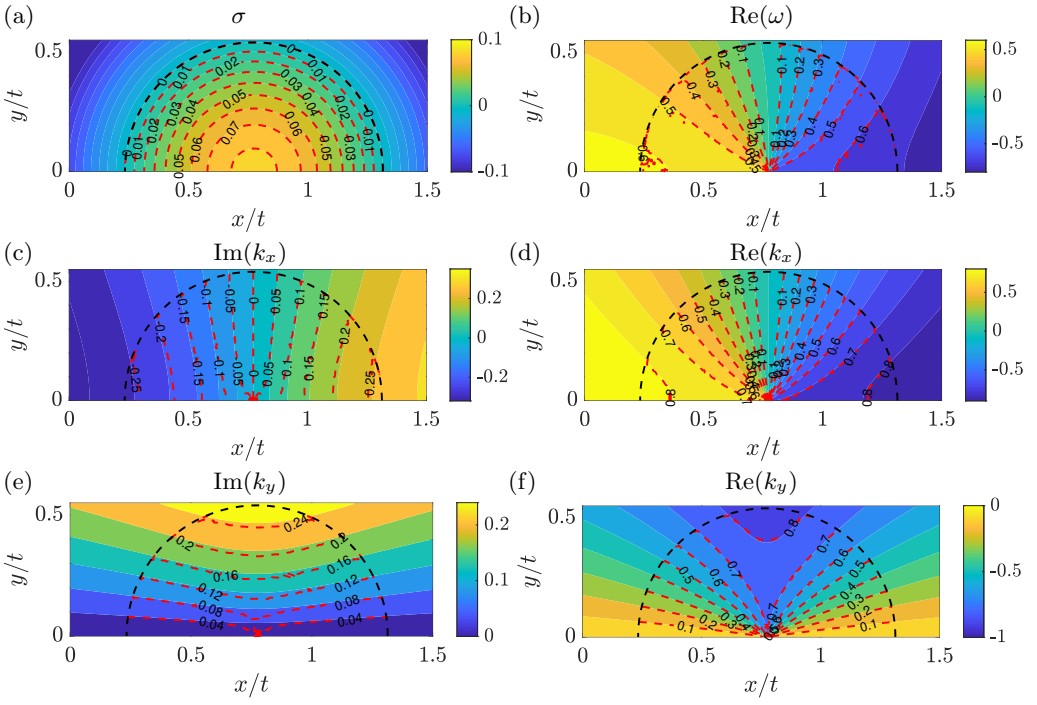

FIGURE 4. Long-time asymptotic properties of the two-dimensional linear impulse response in the absence of deposition, for $u = 0.77$, as functions of x/t and y/t. The colored iso-contour plots represent the analytical results of Section 3.2. (a) spatio-temporal growth rate. (b) Real part of the complex frequency. (c) Imaginary part of the streamwise wavenumber. (d) Real part of the streamwise wavenumber. (e) Imaginary part of the spanwise wavenumber. (f) Real part of the spanwise wavenumber. The black dashed line identifies the region $\sigma = 0$. The red dashed lines denote the results of the post-processing algorithm described in Section 4.

where $\omega'' = \omega - k_x x/t - k_y y/t$. The resulting values of k_x, k_y and ω'' for each ray $(x/t, y/t)$ allow to reconstruct the linearized dynamics of the wavepacket.

The evaluation of the saddle points is performed in MATLAB, by using the built-in function *fsolve* that solves simultaneously for the saddle points in the two complex planes k_x and k_y using the dispersion relation eq. (3.2). The initialization is based on the solution of the one-dimensional case documented in Brun *et al.* (2015) for $(x/t, y/t) = (0, 0)$, which corresponds to the maximum temporal growth rate in the dispersion relation and is a contributing saddle point according to Barlow *et al.* (2017). The solution at different $(x/t, y/t)$ is obtained using as initial guess the previously calculated value.

The asymptotic properties for $u = 0.77$ are reported in fig. 4. We report only positive values of y/t, since ω'', ω and k_x are symmetric with respect the axis $y/t = 0$, while k_y is antisymmetric. The iso-contours of the spatio-temporal growth rate $\sigma = \mathrm{Im}(\omega'')$ (fig. 4(a)) are concentric circles that propagate from a center at $(x/t = u, y/t = 0)$. The maximum value $\sigma = 1/12$ is located at the center and coincides with the maximum of the dispersion relation eq. (3.2). Increasing the distance from the center, the values of σ decrease. At a distance from the center of ≈ 0.54, the spatio-temporal growth rate is zero, and becomes negative at larger distances. The full description of the asymptotic properties is completed with the results in fig. 4(b-f). The real part of the complex frequency Re(ω) (fig. 4(b)) is characterized by positive values in the upstream part of the wavepacket and by negative values in the downstream part. The transition region

where $\mathrm{Re}(\omega) = 0$ is located at $x/t = u$, and the transition becomes more abrupt whilst decreasing y/t, with a discontinuity at $y/t = 0$. This discontinuity can be observed also in the real parts of the streamwise (fig. 4(d)) and spanwise (fig. 4(f)) wavenumbers, while the corresponding imaginary parts (fig. 4(c,e)) are zero.

According to the spatio-temporal analysis approach (Van Saarloos 2003), the front is defined by the region where $\sigma = 0$. In the one-dimensional case the front is defined only by a value of x/t, while in two-dimensions by couples $(x/t, y/t)$. From the analysis, it results that the front of the wave-packet is a circle of radius ≈ 0.54 centered around $(x/t = u, y/t = 0)$. This value agrees with the absolute-convective instability transition predicted by Brun *et al.* (2015) for the one-dimensional case. Since the center of the wavepacket is located at $x/t = u$, and the front is a circle of radius 0.54 (independent of u), the first case in which the spatio-temporal growth rate is non-negative at $x/t = 0$ is when $u = 0.54$. As the linear advection velocity decreases, the unstable region invades negative values of x/t, i.e. upstream of the initial impulse position, and the flow is said to be absolutely unstable (Huerre & Monkewitz 1990).

The above-performed analytical spatio-temporal analysis could be in principle performed also in the presence of the deposition process. Nevertheless, the possible presence of multiple saddle points to be identified and the discrimination of upstream and downstream propagating branches related to the different saddle points makes the problem arduous to tackle theoretically. We therefore propose a numerical approach, which presents some originalities and interesting perspectives. The analytical results of this section will be used to validate the numerical algorithm and as a reference point when restoring the coupling with the deposition process.

4. Numerical approach based on the monogenic signal

4.1. *The Riesz transform and the monogenic signal*

In this section, we introduce the mathematical tools necessary for the spatio-temporal analysis of the impulse response from the linear simulations. Numerical analyses of the linear impulse response have been already performed in literature (Delbende *et al.* 1998; Delbende & Chomaz 1998; Gallaire & Chomaz 2003), where the asymptotic properties along one single direction were studied. The study of the asymptotic properties of a one-dimensional wavepacket is based on the introduction of the analytic signal (Delbende *et al.* 1998), which is the complex continuation of a real signal. The analytic signal is derived using the *Hilbert transform*, which corresponds to a phase shift of $-90°$ and $+90°$ respectively to the positive and negative Fourier components of a function $g(x)$, i.e. the Hilbert transformed signal reads:

$$\mathcal{H}g(x) = H_x \star g(x), \tag{4.1}$$

where H_x is a Heaviside filter characterized by the Fourier transform $\hat{H}_x(k_x) = -\mathrm{i}\,\mathrm{sgn}(k_x)$, and the symbol $\star$ denotes the convolution operator. In the Fourier domain, the convolution becomes a product, such that the Fourier tranform of the Hilbert transformed signal reads $\hat{\mathcal{H}g} = -\mathrm{i}\,\mathrm{sgn}(k_x)\hat{g}(k_x)$, where $\hat{g}$ is the Fourier transformed signal. The analytic signal gives access to the envelope and the phase of the wavepacket; indeed, as an alternative to its representation as the two components function $\mathbf{g}_a(x) = (g(x), \mathcal{H}g(x))$, the complex function $g_a(x) = g(x) + \mathrm{i}\mathcal{H}g(x)$ can be defined. The analytic signal g_a is said to be the complex continuation of the real signal and can be rewritten in terms of amplitude and phase $g_a(x) = A\exp(\mathrm{i}\xi)$, where A is the instantaneous amplitude (i.e., the envelope) and ξ the phase of the complex signal. As

explained in detail in the Section 4.2, the knowledge of the envelope of the wavepacket is necessary to analyze the spatial and temporal growth rates, while the phase gives access to the spatial and temporal frequencies.

Our work aims to generalize the approach of Delbende *et al.* (1998) to the two-dimensional case, in the presence of two spatial propagation directions. We introduce the *monogenic* signal, the multi-dimensional generalization of the analytic signal (Unser *et al.* 2009). In literature, there are several attempts to generalize the analytic signal in two-dimensions (Bulow & Sommer 2001; Felsberg & Sommer 2001; Hahn 2003). In this work, we use the definition given by Unser *et al.* (2009), based on the multi-dimensional generalization of the Hilbert transform, the *Riesz transform* (Stein & Weiss 2016). In the two-dimensional case, in analogy to the Hilbert transform, the Riesz operator transforms the scalar signal $g(x, y)$ to the vector signal $\mathbf{g}_R(x, y)$ that reads

$$\mathbf{g}_{\mathrm{R}}(x,y) = \begin{pmatrix} g_{\mathrm{R1}}(x,y) \\ g_{\mathrm{R2}}(x,y) \end{pmatrix} = \begin{pmatrix} H_x * g(x,y) \\ H_y * g(x,y) \end{pmatrix}, \tag{4.2}$$

where $*$ denotes the convolution operator in two dimensions. The functions H_x and H_y are two Heaviside filters characterized respectively by the Fourier transforms $\hat{H}_x(k_x, k_y) = -\mathrm{i}k_x/k$ and $\hat{H}_y(k_x, k_y) = -\mathrm{i}k_y/k$, and they are the generalization of the one dimensional Heaviside filter to two spatial directions. In analogy to the Hilbert transformed signal, we consider a definition of the Riesz transformed signal that combines the two components in one scalar signal (Unser *et al.* 2009) :

$$\mathcal{R}g(x,y) = g_{\mathrm{R1}}(x,y) + \mathrm{i}g_{\mathrm{R2}}(x,y), \tag{4.3}$$

which in the Fourier domain reads:

$$\hat{\mathcal{R}}g(k_x,k_y) = \frac{(-\mathrm{i}k_x + k_y)}{k}\hat{g}(k_x,k_y), \tag{4.4}$$

where $\hat{g}$ is the two-dimensional Fourier transform of the signal. Note that at $k_x = k_y = 0$ the Fourier transform of the Riesz transformed signal is singular and the regularization assumes zero value at the origin. We then introduce the monogenic signal as the three-components function:

$$\mathbf{g}_m(x,y) = (g(x,y), \mathrm{Re}(\mathcal{R}g(x,y)), \mathrm{Im}(\mathcal{R}g(x,y))) = (g, g_{R1}, g_{R2}) \tag{4.5}$$

According to Unser *et al.* (2009), the relation between the Riesz and the Hilbert transforms along the (x, y) directions can be seen as the equivalent between the definition of gradient and partial derivatives. The quantity $r = \sqrt{g_{R1}^2 + g_{R2}^2} = |\mathcal{R}g|$ identifies the maximum response of the directional Hilbert operator

$$\max_{\psi}\{\mathcal{H}_\psi g\} = \max_{\psi}\left\{\mathrm{Re}\left(e^{-\mathrm{i}\psi}\mathcal{R}g\right)\right\} \tag{4.6}$$

along the direction d_ψ given by the angle $\psi = \mathrm{atan}(g_{R2}/g_{R1})$. The instantaneous amplitude (i.e. the envelope of the signal) is given by

$$\mathrm{A} = \sqrt{g^2 + g_{R1}^2 + g_{R2}^2}, \tag{4.7}$$

and the phase by

$$\xi = \mathrm{atan}(\sqrt{g_{R1}^2 + g_{R2}^2}/g). \tag{4.8}$$

This decomposition allows us to write the monogenic signal along d_ψ in the form

$$\tilde{g}(x,y,t) = \mathrm{A}\exp(\mathrm{i}\xi). \tag{4.9}$$

The amplitude A represents the envelope of the signal and ξ the phase along the direction d_ψ. Note that eq. (4.9) is valid only when amplitude and phase of the signal can be demodulated (Delbende *et al.* 1998). This is valid when the variations of the envelope occur at a scale much larger than that governing of the oscillations. The representation in eq. (4.9) is the two-dimensional equivalent of the analytic signal (Delbende *et al.* 1998) and identifies in $\tilde{g}$ the complex continuation of the two-dimensional real signal g.

4.2. *Large time asymptotic properties*

In this section, we derive the asymptotic properties of the wavepacket by following the same procedure outlined in Delbende *et al.* (1998). According to Section 3.2, the complex Green Function reads:

$$\tilde{g} \sim \exp[\mathrm{i}\,(k_x x + k_y y - \omega t)]/t, \tag{4.10}$$

where the asymptotic properties k_x, k_y and ω depend on x/t and y/t.

The linear simulations of the impulse response give as a result the real signal $g(x, y)$. We thus recover the complex Green function by the analytic continuation of g, i.e. the monogenic signal $\tilde{g}$:

$$\tilde{g} \sim \exp[\mathrm{i}\,(k_x x + k_y y - \omega t)]/t = \mathrm{A}\exp(\mathrm{i}\xi), \tag{4.11}$$

where $\mathrm{A} = |\tilde{g}|$ and $\xi = \arg(\tilde{g})$. Thus, by exploiting the last expression, we can use the monogenic signal $\tilde{g}$ to evaluate the asymptotic properties of the wavepacket. The spatio-temporal growth rate

$$\sigma = \mathrm{Im}(\omega'') = \mathrm{Im}(\omega) - \mathrm{Im}(k_x)x/t - \mathrm{Im}(k_y)y/t = \mathrm{Im}(\omega) - \mathrm{Im}(k_x)v_x - \mathrm{Im}(k_y)v_y, \tag{4.12}$$

which represents the growth of a perturbation along a ray of group velocities $(x/t, y/t) = (v_x, v_y)$, is obtained by applying the logarithm operator to the absolute value of eq. (4.11)

$$|\tilde{g}| \sim \exp(\sigma t)/t = \mathrm{A} \quad \rightarrow \quad \sigma t - \ln(t) \sim \ln(A) \tag{4.13}$$

and thus by evaluating the derivative with respect to time of the resulting expression, for $(x/t = \mathrm{const}, y/t = \mathrm{const})$:

$$\sigma(x = v_x t, y = v_y t) \sim \frac{\mathrm{d}}{\mathrm{d}t}\ln(A(x = v_x t, y = v_y t, t)) + \frac{1}{t}. \tag{4.14}$$

The definition of the spatio-temporal growth rate eq. (4.12) allows us to evaluate the imaginary part of the streamwise and spanwise wavenumbers at each ray $(x/t, y/t) = (v_x, v_y)$ (see Appendix B for details):

$$\mathrm{Im}(k_x(x = v_x t, y = v_y t)) = -\partial_{v_x}\sigma, \tag{4.15}$$

$$\mathrm{Im}(k_y(x = v_x t, y = v_y t)) = -\partial_{v_y}\sigma. \tag{4.16}$$

The real parts of the spatial wavenumbers are retrieved by considering eq. (4.11) and exploiting the definition of phase:

$$\mathrm{Re}(k_x(x = v_x t, y = v_y t)) \sim \partial_x \xi(x = v_x t, y = v_y t), \tag{4.17}$$

$$\mathrm{Re}(k_y(x = v_x t, y = v_y t)) \sim \partial_y \xi(x = v_x t, y = v_y t). \tag{4.18}$$

Alternatively, still exploiting the logarithm of eq. (4.11), a direct evaluation of the real and imaginary parts of the spatial wavenumbers from the complex monogenic signal can be performed:

$$k_x \sim -\mathrm{i}\partial_x \ln(\tilde{g}(x = v_x t, y = v_y t)), \tag{4.19}$$

$$k_y \sim -\mathrm{i}\partial_y \ln(\tilde{g}(x = v_x t, y = v_y t)). \tag{4.20}$$

In this work, we adopted this technique to evaluate the streamwise and spanwise wavenumbers. The temporal growth rate is obtained from the knowledge of the spatio-temporal growth rate and the imaginary part of the wavenumbers:

$$\mathrm{Im}(\omega) = \sigma + \mathrm{Im}(k_x)x/t + \mathrm{Im}(k_y)y/t. \tag{4.21}$$

The real part of the complex frequency is, by definition, the temporal derivative of the phase ξ:

$$\mathrm{Re}(\omega)(x/t, y/t, t) \sim -\partial_t \xi(x/t, y/t, t). \tag{4.22}$$

Note that in this case the derivative with respect to the time is evaluated in a relatively short time interval, without following the rays $x/t = v_x$ and $y/t = v_y$ (Delbende *et al.* 1998). Moreover, the sign of the spatial frequencies cannot be recovered from the analysis, since we are post-processing a real signal. In the following, we will consider positive values for the real parts of the complex frequency and spatial wavenumbers.

4.3. *Numerical procedure and validation*

The analytical developments derived in the previous sections aim at describing the asymptotic behavior for $t \to \infty$ using numerical simulations at finite times. Besides, eq. (4.9) assumes that the amplitude and the phase of the signal subject to the Riesz transform can be demodulated, i.e. that a separation of scales between the variations of the envelope and the oscillations subsists. In this section, we verify the numerical procedure and the validity of the assumptions using as a test case the analytical solution described in Section 3.2. The post-processing algorithm is validated against the theoretical results of the impulse response in the absence of substrate variations. The numerical implementation is based on MATLAB. The linear response is computed using eq. (3.1) subjected to the a Gaussian initial condition that mimics the Delta function behavior:

$$\eta(x, y, 0) = \eta^0(x, y, 0) = \exp[-(x^2 + y^2)/2\varsigma^2]. \tag{4.23}$$

with $\varsigma = 1$; no appreciable changes in the response have been observed for $\varsigma < 1$.

The numerical steps for the post-processing are the following. We apply the two-dimensional Fourier transform to the linear response at different times via the built-in MATLAB function *fft2*. We obtain the Riesz transformed signal by eq. (4.4) . The inverse Fourier transform is applied (via the built-in MATLAB function *ifft2*) and we build the monogenic signal in the physical space, for different times, according to eq. (4.9). We evaluate the spatio-temporal growth rate by eq. (4.12), using the monogenic signals evaluated at different times. We then obtain the streamwise and spanwise wavenumbers by a finite difference expression of eq. (4.19-4.20), and then the temporal growth rate by a finite difference approximation of eq. (4.21). Finally, the real part of the complex frequency is recovered from eq. (4.22) using the computed monogenic signals at different times.

We evaluate the derivatives using first-order finite differences. A convergence analysis has been performed on the number of collocation points and the order of the finite differences for the derivatives, and we observed the convergence of the results already for a domain of $L_x = L_y = 1000$ and $N_x = N_y = 1001$. The odd number of points is necessary to have also the zero frequency $k_x = k_y = 0$, where the transfer function of the Riesz transform is singular and has to be regularized imposing the zero value. The results are averaged at different times (Lerisson 2017). We consider a time step of $\Delta t = 15$ for the evaluation of the spatio-temporal growth rate, from $t = 200$ to $t = 350$. At each

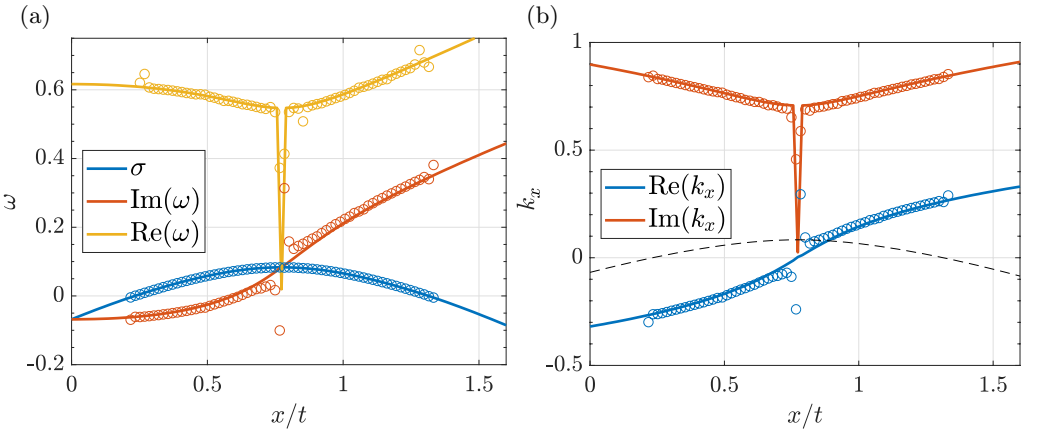

FIGURE 5. Comparison of the long-time asymptotic properties of the two-dimensional linear impulse response in the absence of deposition ($u = 0.77$) as functions of x/t, for $y/t = 0$. The solid lines and the dots denote respectively the analytical (Section 3.2) and numerical approaches (Section 4). (a) spatio-temporal growth rate, imaginary and absolute value of the real part of the complex frequency. (b) Imaginary and absolute value of the real part of the streamwise wavenumber. The black dashed line denotes the values of σ.

time, the real part of the complex frequency is evaluated using a time step of $\delta t = 0.01$ (Delbende *et al.* 1998).

In fig. 4 we also report a comparison of the post-processing algorithm (red dashed lines) against the results of the saddle points analysis (colored iso-contours). The results agree with those obtained from the saddle points approach. The spatio-temporal growth rate (fig. 4(a)) is well described by the numerical post-processing, and the front of the wavepacket is well captured. The other variables well agree with the analytical solution. Fig. 5 shows the results for the temporal properties and the streamwise wavenumber as functions of x/t, at $y/t = 0$. The comparison reveals a good agreement, except in the center of the wavepacket where the analytical solution is discontinuous. The difference can be imputed to a transient effect at the center of the wavepacket, which is reduced as time increases. Note that the analytical solution of Section 3.2 is rigorously valid as $t \to \infty$. Nevertheless, in the numerical simulations, there is a practical limit in the final time related to the numerical noise. The maximum ratio between the smaller and greater values in the simulations is limited to 16 decades, for the *double* precision (Trefethen & Bau III 1997). Therefore, we cannot go beyond the final time above defined, i.e. $t = 350$. Despite the presence of a discontinuity in the center of the wavepacket, the numerical procedure well captures the structure of the solution. Concerning the spatio-temporal growth rate, the maximum error from the theoretical value is around $\Delta = 2 \times 10^{-3}$, which means a percentual error of 2.5%. The edges of the wavepacket well agree with the analytical solution. We conclude that our post-processing algorithm is able to capture the spatial structure of the asymptotic properties, making it suitable for the study of the impulse response in the presence of the deposition process.

5. Linear response in the presence of the deposition process

5.1. *Dispersion relation*

In this section, we briefly study the temporal stability properties in the presence of the deposition process. Following the linear stability analysis approach, we assume the normal mode expansion

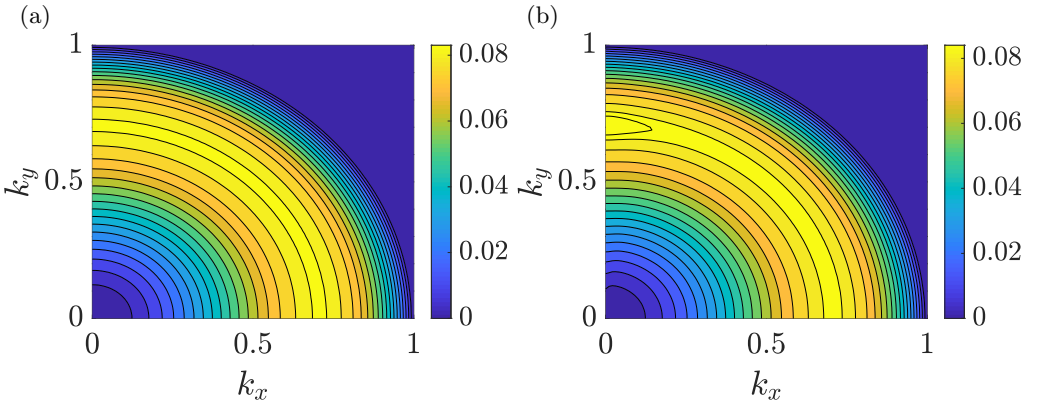

FIGURE 6. Temporal growth rate $\mathrm{Im}(\omega)$ from the dispersion relation with deposition (eq. 5.2) as a function of (k_x, k_y), for (a) $C = 10^{-5}$, (b) $C = 10^{-3}$.

$$[\eta, \eta^0]^T = [\eta, \eta^0]^T \exp[\mathrm{i}\,(k_x x + k_y y - \omega t)]. \tag{5.1}$$

It is worth to underline that this decomposition for the substrate thickness assumes that the temporal growth due to the presence of the flat film is much slower than the one related to the Rayleigh-Taylor instability. The deposition constant C. describes the growth in the absence of patterns in the fluid film. The characteristic time scale of this process has to be large enough so as to the variations of the baseflow are negligible as the instability occurs. Under these conditions, a separation of scales between the speleothem growth and the Rayleigh-Taylor instability subsists. Since C is already adimensionalized with the characteristic time scale of the Rayleigh-Taylor instability, we restrict ourselves to the case $C < 10^{-3}$. In these conditions, we can safely assume the ansatz eq. (5.1).

We introduce the normal mode decomposition in the equations for the linearized dynamics eq. (2.8), leading to the dispersion relation which relates the complex frequency ω to the wavenumbers (k_x, k_y) for the coupled hydrodynamic-deposition problem:

$$\omega = \frac{\omega^H}{2} \pm \sqrt{\left(\frac{\omega^H}{2}\right)^2 - \frac{\check{C}}{3}\left(k^2 - k^4\right)}, \tag{5.2}$$

where ω^H is the complex frequency in the absence of substrate variations, eq. (3.2).

The dispersion relation eq. (5.2) is the analogous of the one reported in Bertagni & Camporeale (2017) in the absence of inertial effects. Two branches of the dispersion relation are identified. One branch is always damped while the other one tends to the hydrodynamic case as C goes to zero. The dynamics is governed by two adimensional parameters, the linear advection velocity u and the deposition constant C. A preliminary analysis of the influence on the dispersion relation for a large range of u did not show any appreciable effect on the temporal growth rate of perturbations, for fixed deposition constants $10^{-10} < C < 10^{-3}$. For computational reasons, it is not convenient to consider extremely large values of u, as large as those that can be found in limestone caves ($l_c/h_N \sim 270$, i.e. $u \sim 10^2$), since the advection of perturbations will require the use of irrealistic extremely large computational domains for the numerical simulations, while the physics of the traveling wavepacket would not change significantly. For these reasons, we focus on the case $u = 0.77$ and $\theta = 55°$, and we study the effect of the deposition constant C.

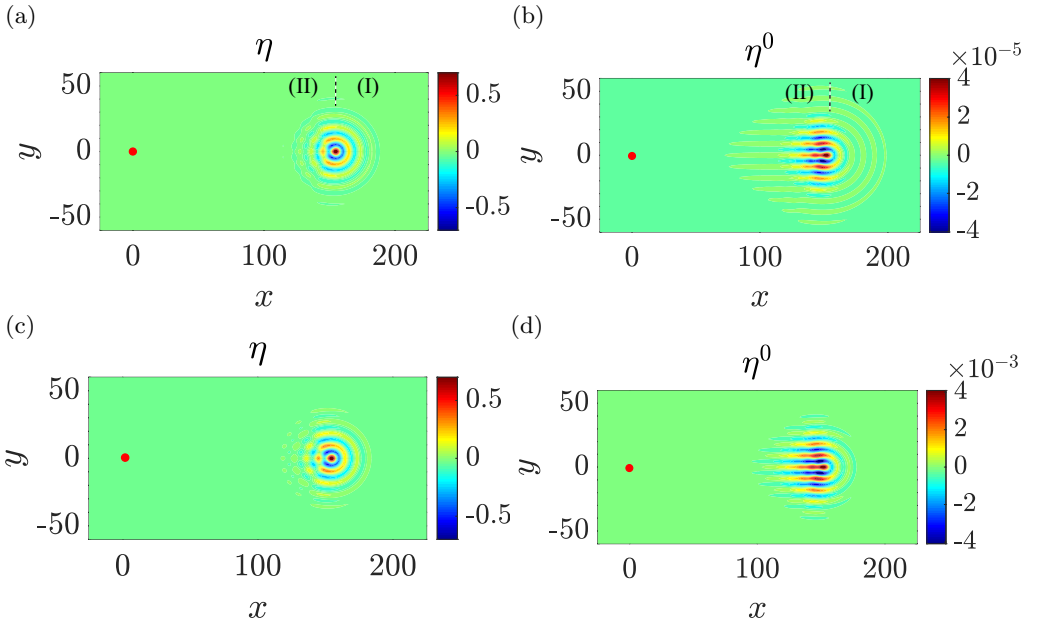

FIGURE 7. Linear impulse response (eq. 2.8), for $u = 0.77$, at $t = 200$. (a-b) $C = 10^{-5}$, (a) fluid film and (b) substrate thickness. (c-d) $C = 10^{-3}$, (c) fluid film and (d) substrate thickness. Results are rescaled with the maximum fluid thickness for visualization purposes. The red dots denote the initial impulse location.

In fig. 6 we report the temporal growth rate $\mathrm{Im}(\omega)$ as a function of (k_x, k_y), for different values of the deposition constant. For $C = 10^{-5}$, the temporal growth rate is analogous to the case without deposition, and no appreciable anisotropies are observed. At very high values of the deposition constant, $C = 10^{-3}$, the iso-values are concentric circles in most of the (k_x, k_y) plane, but there is a small region located close to $k_x = 0$ where the growth rate is slightly higher (the difference is of order 10^{-3}). The isotropy is broken, and spanwise structures (*rivulets*) experience a slightly larger growth than the streamwise structures (*waves*), as already pointed out in Bertagni & Camporeale (2017).

Nevertheless, the small anisotropy in the dispersion relation may be not sufficient to completely characterize a linear selection of streamwise structures in the deposition process that should arise also for low values of the deposition constant, in the range defined by Camporeale (2015). Moreover, the complex form of the dispersion relation does not highlight how the deposition process influences the spatio-temporal growth of perturbations, and thus it does not shed light on the physics underlying the phenomenon. We therefore focus on the response of the system to a localized initial perturbation, i.e. the Green function.

5.2. *Numerical impulse response*

In this section, we focus on the spatio-temporal analysis of the linear impulse response, both on the substrate and in the fluid film, in the presence of the deposition process (eq. (2.8)). We consider two representative values of the deposition constant which cover the physical range indicated by Camporeale (2015), $C = 10^{-5}$ and $C = 10^{-3}$. Figure 7 shows the linear impulse response in terms of fluid and substrate thickness, at $t = 200$. We recall that in Section 3 we observed that the fluid thickness response in the absence of substrate variations was characterized by concentric circles. The fluid film thickness

(fig. 7(a,c)) is characterized by a quite similar structure, albeit some differences can be highlighted. While in the downstream part (I) we observe circular iso-values for η, the pattern in the upstream part (II) is more intricate.

The substrate thickness (fig. 7(b,d)) presents similar peculiarities. The iso-values in the downstream part are circular, while in the upstream part streamwise aligned structures are present. The region in which streamwise structures dominate roughly corresponds to the region upstream of the maximum film thickness. These structures grow as higher values of the deposition constant are considered. As a consequence, we observe a more perturbed pattern in the fluid film.

The isotropy breaking in the fluid film is related to the presence of deposited streamwise structures in the upstream part of the wavepacket. While in the downstream part the hydrodynamics dominate the pattern with an isotropic structure reminiscent of the case without deposition (Section 3), observed also in the substrate thickness, in the upstream part we observe an interaction between the hydrodynamics and the deposition process.

As the impulse travels, it leaves behind a substrate pattern characterized by predominant streamwise structures. From a physical point of view, this may be explained by the fact that waves are structures that are advected away with the flow, while rivulets are not. Furthermore, it has to be remembered that the deposition law is linear with the film thickness (see eq. 2.6). The growth of substrate disturbances is overposed with the classical growth in the presence of a flat film, i.e. the substrate thickness is always increasing, but this is not obvious for the perturbation η^0. Since waves are traveling structures (i.e., they are oscillating at fixed locations), the linearized deposition law is sequentially increasing and decreasing the substrate perturbation with respect to the linear growth in time, then leading to a much smaller effect on the deposition process. On the contrary, rivulets are not traveling structures. The substrate perturbation always increases or decreases, since there is no advection of the fluid structures along the spanwise direction. As a consequence of the passage of the wavepacket, predominant streamwise structures are deposited on the substrate.

5.3. *Large time behavior of the impulse response*

In this section we apply the post-processing algorithm, introduced in Section 4, to the two cases of fig. 7. According to the decomposition of eq. (5.1), the analysis of the asymptotic properties can be applied to both variables. The difference in the patterns observed in fig. 7 are related to the different eigenvectors $[\hat{\eta}, \hat{\eta}^0]$. In the following, we consider the fluid thickness for the evaluation of the asymptotic properties. However, the observed physical results are not affected by this choice.

In fig. 8(a) we report the spatio-temporal growth rate obtained from the post-processing algorithm, for $C = 10^{-5}$. The spatio-temporal growth rate is greater than zero in a region downstream of the initial impulse position (III). The unstable region spreads in the $(x/t, y/t)$ plane within a region roughly defined by a front angle $\phi \simeq 36.5°$. In the downstream part of the wavepacket (I), we observe circular iso-values of the spatio-temporal growth rate, which decreases moving away from the value of $(x/t = u, y/t = 0)$. The two regions interact in the region just upstream of the maximum spatio-temporal growth rate position (II). The real part of the complex frequency (fig. 8(b)) presents the same structure of the spatio-temporal growth rate. In the region downstream of the initial impulse location, both the real and imaginary parts of the complex frequency are close to zero.

A complete characterization of the asymptotic behavior of the impulse response requires also the evaluation of the spatial asymptotic properties k_x and k_y, which are reported in fig. 8(c-f). Downstream of the initial impulse location, all the spatial proper-

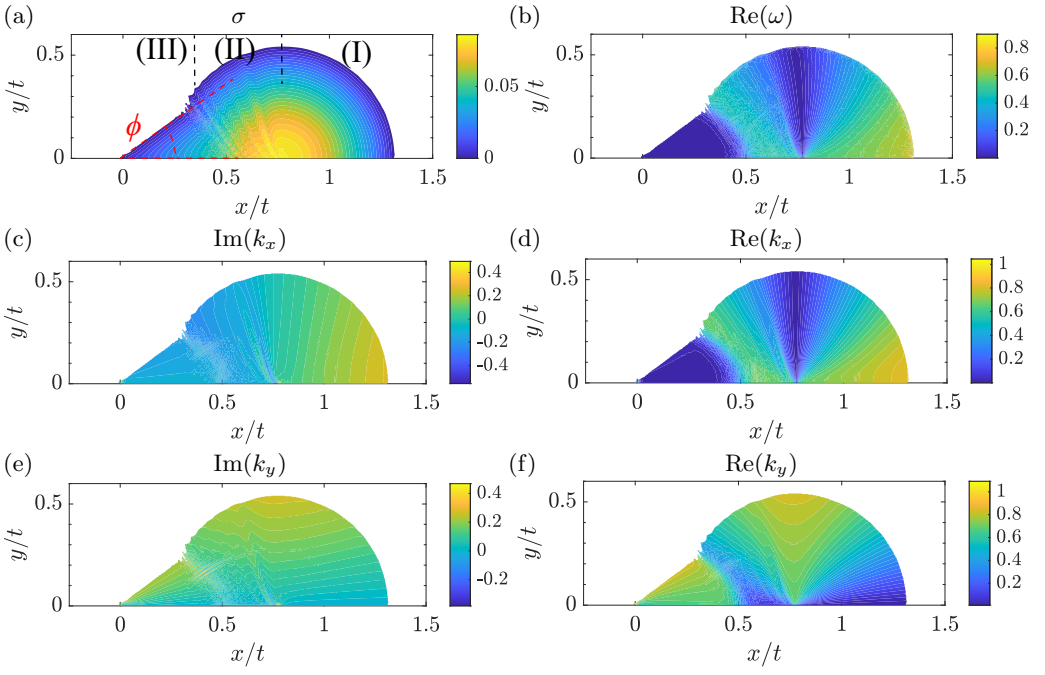

FIGURE 8. Asymptotic properties from the post process algorithm (Section 4), for $u = 0.77$ and $C = 10^{-5}$. (a) spatio-temporal growth rate. (b) Real part of the complex frequency. (c) Imaginary part of the streamwise wavenumber. (d) Real part of the streamwise wavenumber. (e) Imaginary part of the spanwise wavenumber. (f) Real part of the spanwise wavenumber.

ties iso-values are approximately rays that propagate from the initial impulse position. Interestingly, the real part of the streamwise wavenumber is very small, i.e. $\mathrm{Re}(k_x) \sim 10^{-2}$. Moreover, at $y/t = 0$, $\mathrm{Re}(k_y) \simeq 1/\sqrt{2}$, while in the absence of deposition it was zero except in the singular point at the center of the wavepacket.

The same behavior is found in the case $C = 10^{-3}$ (reported in Appendix C), but the front downstream of the initial impulse position is more curved. Moreover, the region in which the two patterns interact is displaced downstream.

The present analysis reveals that there are three regions in the spatio-temporal impulse response. The region (I) is characterized by asymptotic properties whose distribution is very similar to the case in the absence of substrate variations, studied in Sec 3.2. In the region (III), streamwise structures dominate. Since in the region just downstream of the initial impulse location, the complex growth rate is close to zero, the pattern is almost steady. Moreover, the analysis of the spatial asymptotic properties reveals that streamwise aligned structures dominate, since $\mathrm{Re}(k_x) \sim 10^{-2}$ and $\mathrm{Re}(k_y) \sim 1/\sqrt{2}$. The other spatial asymptotic properties are almost constant for $y/x = \text{const}$ since the iso-values are rays that propagate from the initial impulse position. In region (II), the two regions (I) and (III) interact, and it is best observed in the fluid film response (fig. 7), where the substrate presents non negligible values of the thickness compared to the fluid film. In this region, due to the high values of the fluid film thickness, we observe a strong deposition and an increase of the substrate thickness.

We therefore identified two linear mechanisms that could lead to the emergence of draperies structures on the substrate. First, the advection of oscillating perturbations along the streamwise direction promotes the deposition of drapery-like structures rather than wave patterns on the substrate (*ripples*). This interpretation confirms the observa-

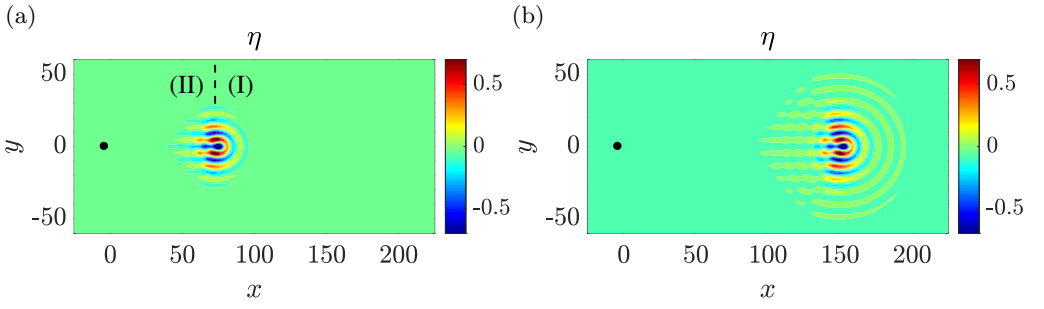

FIGURE 9. Linear fluid film response eq. (2.8) (rescaled with the maximum value) in the presence of a steady defect (i.e. $C = 0$) located at $(x = 0, y = 0)$, for $u = 0.77$, (a) $t = 100$, (b) $t = 200$. The black dots denote the steady defect location.

tion of slightly higher growth rates for spanwise perturbations in the two-dimensional dispersion relation of Bertagni & Camporeale (2017). This first mechanism strongly enhances the growth of draperies structures in the region just upstream of the maximum thickness, which is advected away with time. The second mechanism was highlighted thanks to the post-processing algorithm, which shows the presence of another region in which the perturbation grows, absent in the case without substrate variations of Section 3.2. The presence of the initial defect that grows without being advected, creates a quasi-steady region characterized by streamwise structures both in the fluid film and on the substrate. The second mechanism appears to be dominant in the regions in which the isotropic response has been advected away. In the following, we investigate the hydrodynamic origin of this second source of anisotropy.

6. Linear response in the presence of a steady defect without deposition process

6.1. *Numerical response and large-time asymptotics*

In this section, we provide an additional analytical insight to better understand the physical mechanisms underlying the response in the presence of the deposition process. We consider the linear response of the thin film (eq. 2.8) in the presence of a steady defect (i.e. $C = 0$) of the form:

$$\eta^0(x, y, t) = \exp[-x^2/2 - y^2/2], \tag{6.1}$$

together with the initial condition for the fluid thickness $\eta(x, y, 0) = 0$.

The wavepacket (fig. 9), in the downstream part (I), is characterized by the isotropic structure typical of the temporal response (fig. 3,7), as described in detail in Section 3.2. Nevertheless, in the upstream part (II) we observe streamwise structures more pronounced than in the case of the impulse response in presence of deposition (described in Section 3.2), since the initial condition differs from a steady defect as it is characterized by an impulse both in the fluid film and on the substrate.

The asymptotic properties (fig. 10) resulting from the post-processing algorithm present a spatial structure analogous to the case in the presence of deposition reported in fig. 8. In the region (III), downstream of the initial impulse location, the iso-values are rays that propagate from $(x/t, y/t) = (0, 0)$. Both real and imaginary parts of the complex frequency are zero in the region downstream of the steady defect, and the real part of the streamwise wavenumber is of order 10^{-2}.

The steady defect analysis confirms that the structure of the wavepacket is mainly

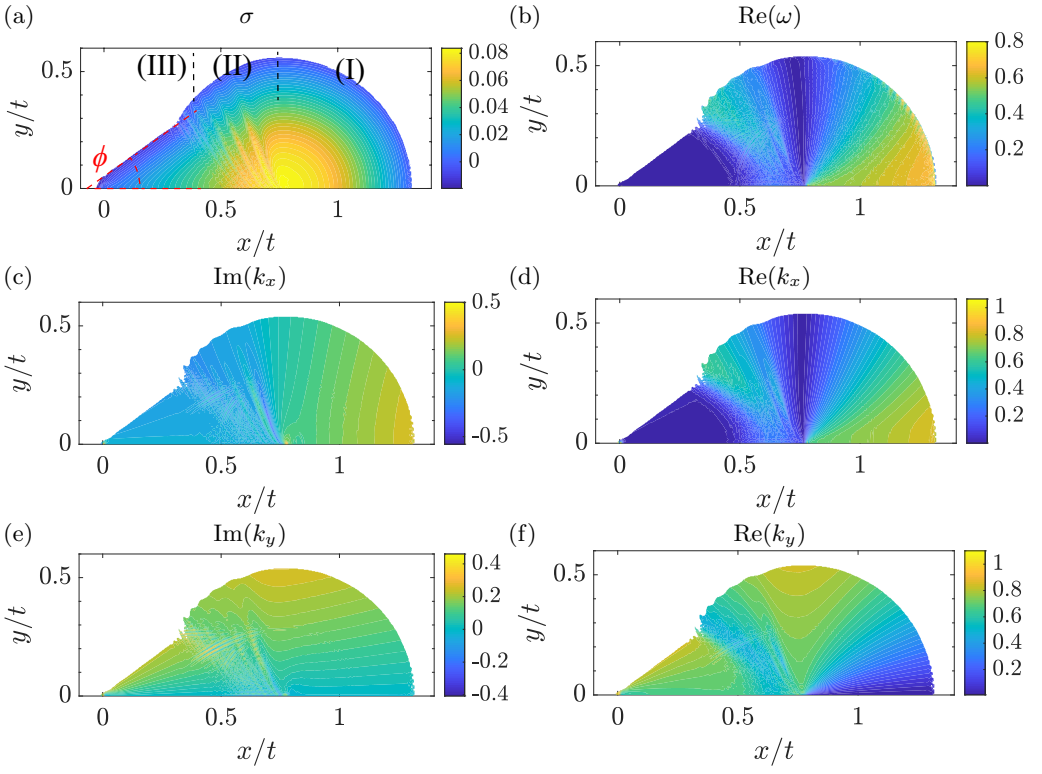

FIGURE 10. Long-time asymptotic properties from the post process algorithm (Section 4) of the two-dimensional linear response to steady defect in the absence of deposition, for $u = 0.77$. (a) spatio-temporal growth rate. (b) Real part of the complex frequency. (c) Imaginary part of the streamwise wavenumber. (d) Real part of the streamwise wavenumber. (e) Imaginary part of the spanwise wavenumber. (f) Real part of the spanwise wavenumber.

driven by hydrodynamic effects. Moreover, the region downstream of the obstacle is steady because $\omega = 0$ and originates from the presence of the steady defect. Since the asymptotic properties are rays that propagate from the center, the properties of the steady pattern are constant at fixed y/x. This invariance suggests that the response can be evaluated in the context of a steady pattern asymptotic analysis, introduced in Lerisson *et al.* (2020) for the front analysis of a propagating steady wavepacket, known as *spatio-spatial* stability analysis.

6.2. *The two-dimensional steady Green function*

In this section, we analytically derive the Green function for a steady defect. The approach is based on the spatio-temporal analysis introduced in Section 3.2, but we focus on the growth in space of a steady wavepacket. We can thus make an analogy to the classical one-dimensional analysis (Van Saarloos 2003): the (x, y) directions play the role of space and time.

Following Hayes *et al.* (2000), we introduce the total free surface elevation $\eta_t = \eta + \eta^0$. We seek for the solution of the following problem:

$$u\partial_x \eta_t + \frac{1}{3}\left[\nabla^2(\eta_t) + \nabla^4(\eta_t)\right] = -u\partial_x \eta^0 = f(x, y). \tag{6.2}$$

The impulse is located in the position $y/x = 0$, i.e. the Green function $\tilde{g}_s(x, y)$ solves the

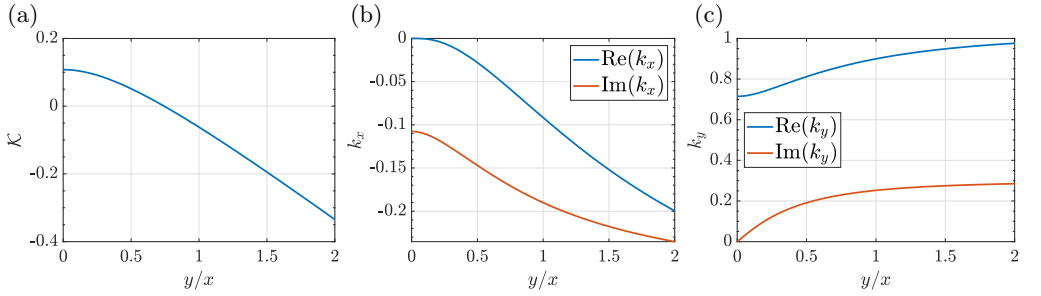

FIGURE 11. Analytical asymptotic properties for the steady two-dimensional Green function. (a) Spatio-spatial growth rate as a function of y/x. (b) Streamwise wavenumber and (c) spanwise wavenumber resulting from the analytical steady response, as functions of y/x.

steady problem:

$$u\partial_x\eta_t + \frac{1}{3}\left[\nabla^2(\eta_t) + \nabla^4(\eta_t)\right] = \delta(x)\delta(y). \tag{6.3}$$

The solution in the presence of a localized defect η_t is found using the property of the Green function, i.e. $\eta_t = \tilde{g}_s * f$, where $*$ is the convolution operator. Since we consider the response to a steady localized defect $f(x,y) = \partial_x[\delta(x)\delta(y)]$. Using the properties of the Delta function and integrating by parts, we obtain that the solution reads:

$$\eta_t = u\partial_x\tilde{g}_s(x,y) \tag{6.4}$$

The solution $\tilde{g}_s$ is found using the same approach of the spatio-temporal stability analysis, where now we have the direction $x \to \infty$. The Green function for steady defect can be expressed as:

$$\tilde{g}_s(x,y) \sim \hat{g}\exp(k_x x + k_y y)/\sqrt{x} \sim \hat{g}\exp(k'_x x)/\sqrt{x}, \tag{6.5}$$

where $k'_x = k_x + k_y(y/x)$. The solution reads:

$$\eta_t = u\partial_x\tilde{g}_s(x,y) \sim \mathrm{i}uk_x\exp[\mathrm{i}(k_x x + k_y y)]/\sqrt{x}, \tag{6.6}$$

i.e. the asymptotic properties of the total elevation η_t wavepacket are the same of the Green function for $x \to \infty$.

The spatio-spatial analysis is implemented similarly to the spatio-temporal stability analysis outlined in Section 3.2. We look for the steady (i.e. $\omega = 0$) dispersion relation (eq. 3.2) saddle points of $k'_x = k_x + k_y(y/x)$ in the complex k_y plane, varying y/x. The resulting asymptotic properties define the response for each y/x. The method is numerically implemented in MATLAB; we solve for the saddle point using the built-in function *fsolve*. The initial guess is given by the maximum in the steady dispersion relation eq. (3.2) for $y/x = 0$, which is a contributing saddle point according to Barlow *et al.* (2017).

In fig. 11 we report the spatial asymptotic properties as functions of y/x. The spatio-spatial growth rate $\mathcal{K} = -\mathrm{Im}(k'_x)$ (fig. 11(a)) is initially positive and decreases with y/x. Beyond the critical value of $y/x = 0.74$ it becomes negative. Both the real and imaginary parts of the streamwise wavenumber (fig. 11(b)) are negative and decrease with y/x, in opposition to the real and imaginary parts of the spanwise wavenumber (fig. 11(c)), which are positive and increase with y/x.

The unstable region in the (x,y) plane is located where the spatio-spatial growth rate is positive. At low values of y/x, i.e. close to $y = 0$, we observe a positive spatio-spatial growth rate, i.e. perturbations are growing (remember that one writes $\eta_t \sim \exp[\mathrm{i}(k_x x + k_y y)]$). When $\mathcal{K} = 0$ we define the value of y/x beyond which perturbations are damped,

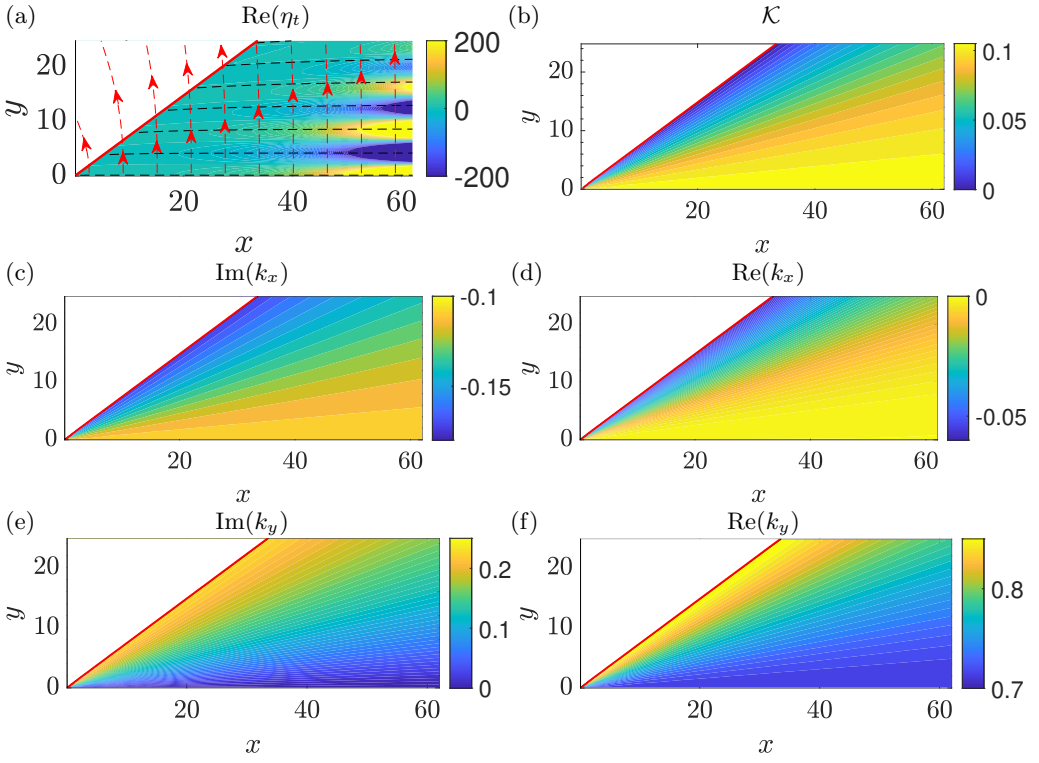

FIGURE 12. Results of the spatio-spatial analysis in the (x, y) plane. (a) Real part of the total free surface elevation η_t obtained from the asymptotic properties. The red and black dashed line denote respectively the streamlines of the wavevector $\mathbf{k} = (\mathrm{Re}(k_x), \mathrm{Re}(k_y))$ and the wavefronts. (b) Spatio-spatial growth rate, (c) imaginary and (d) real parts of the streamwise wavenumber, (e) imaginary and (f) real parts of the spanwise wavenumber. The red line denotes the value of y/x for which $\mathcal{K} = 0$.

that is $y/x = 0.74$. This value of y/x defines a ray in the (x, y) plane, that corresponds to an angle with respect to the x axis of $\phi \simeq 36.5°$, in agreement with the front observed in figures 8 and 10.

These results can be easily visualized in fig. 12, in which we report the real part of the total free surface elevation and the asymptotic properties in the (x, y) plane, in a similar fashion to the previous plots for the spatio-temporal response. The total free surface elevation is characterized by predominant streamwise structures. The steady Green function is growing moving away from the obstacle, in strong contrast to the case of the flow over an incline, in which it is decaying (Decré & Baret 2003; Kalliadasis *et al.* 2000; Hayes *et al.* 2000). The streamlines of the wavevector $\mathbf{k} = (\mathrm{Re}(k_x), \mathrm{Re}(k_y))$ (red dashed lines in fig. 12(a)) are parallel to the y direction at $y = 0$ and slightly bend upstream with y. This slight variation is related to the negative value of the real part of the streamwise wavenumber. The bending of the wavevector streamlines imply that the wavefronts (black dashed lines in fig. 12(a)), orthogonal to the wavevector directions, tend to slightly diverge from the center going downstream.

We now consider the spatio-temporal response observed in Section 6.1. In the steady regions, the spatio-temporal growth rate (Section 3.2) $\sigma = \mathrm{Im}(\omega) - \mathrm{Im}(k_x)x/t - \mathrm{Im}(k_y)y/t = \mathrm{Im}(\omega) + \mathcal{K}x/t$ coincides with the spatio-spatial growth rate rescaled with x/t, i.e. $\sigma = \mathcal{K}x/t$, since $\omega = 0$. In fig. 13 we show the spatio-temporal growth rate obtained from

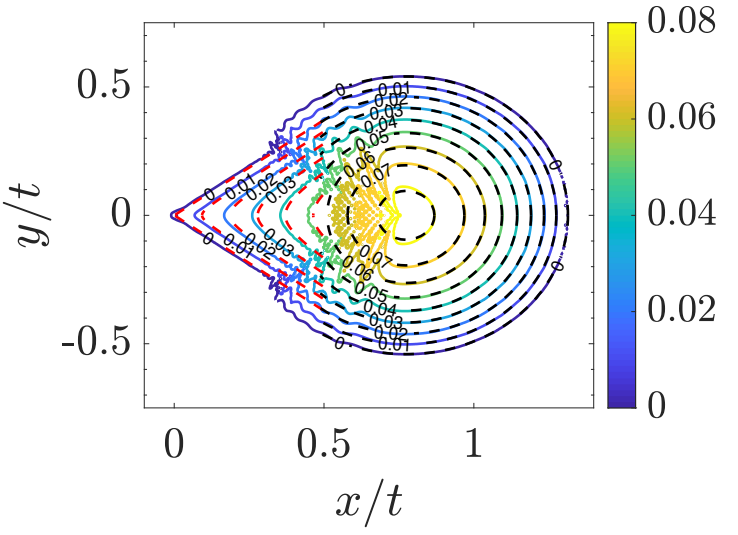

FIGURE 13. Linear response to a steady defect: spatio-temporal growth rate from the post process algorithm of Section 4 (colored iso-contours) and from the saddle points approach of Section 3.2 (black iso-contours) and spatio-spatial growth rate (changed of sign) from the analytical steady approach of Section 6.2 (red iso-contours).

the numerical simulation compared with analytical values of σ and $\mathcal{K}x/t$ respectively obtained from the spatio-temporal (Section 3.2) and spatio-spatial approaches, for $t = 350$. The comparison shows a good agreement between spatio-spatial theory and numerical post-processing in the region downstream of the steady defect. Moreover, the numerical spatio-temporal response well agrees with the spatio-temporal results, in the region downstream of $x/t = u$.

We report in fig. 14 a comparison of the spatial asymptotic properties, at $y/t = 0$. Also in this case, the results are in good agreement; the values of $\mathrm{Re}(k_y)$ are converging to the analytic values as x increases. The small difference in the values can be imputed to the fact that we are considering not large enough values of x close to the obstacle. The saddle point analysis is rigorously valid for $x \to \infty$, and in this case the steady response is present in the range $0 < x < 175$ for the considered time ($t = 350$), which explains the small difference.

Our analysis shows that the temporal response to a steady defect is characterized by the presence of the steady and unsteady ontributions which interact. The steady contribution, which originates from the presence of the steady defect, is not advected away and spreads in the domain as the streamwise coordinate increases. The presence of an initial perturbation gives rise also to a temporal response that is advected away. If enough time is waited, eventually the temporal response is no more present in the field and only the steady response survives, which is characterized by streamwise aligned structures.

We then conclude that the emergence of streamwise structures both on the fluid film and on the substrate in the region just downstream of the initial impulse location is related to the presence of defects on the substrate and it has a linear hydrodynamic origin. This mechanism is predominant in the regions in which the temporal response has been advected away. In the context of morphogenesis of draperies, we thus argue that the response in the presence of the deposition process contains as fundamental ingredients two hydrodynamic effects, one related to the isotropic unsteady response in

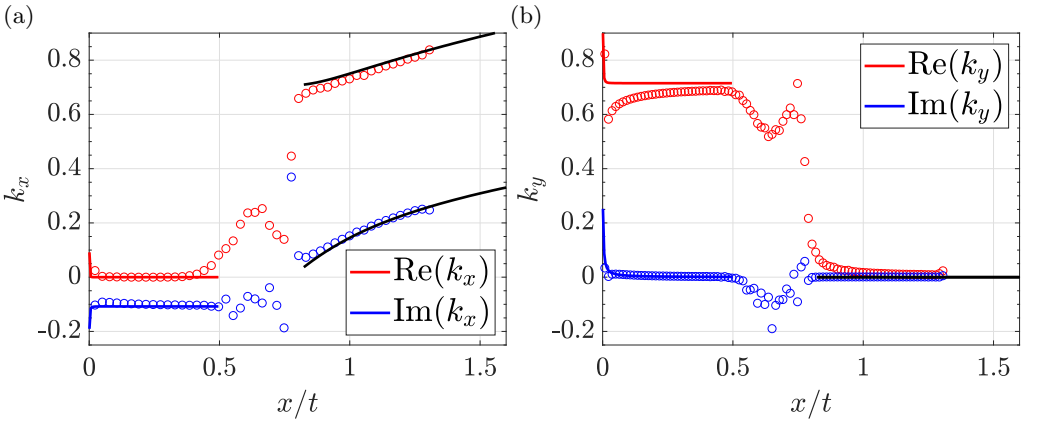

FIGURE 14. Comparison of streamwise (a) and spanwise (b) wavenumbers obtained from the post process algorithm of Section 4 (dots), the analytical approach (colored solid lines) for the response to a steady defect of Section 6.2, and the analytical results of the spatio-temporal analysis of Section 3.2 (black solid lines), on the ray $y/t = 0$.

the absence of substrate variations, and the other one related to the steady response in the presence of a localized defect in the substrate. The deposition process couples these two different hydrodynamic mechanisms, giving rise to predominant draperies structures on the substrate.

7. Non-linear response

The linear response in the presence of the deposition process is compared to non-linear simulations of equations (2.3) and (2.6), for the case $C = 10^{-3}$. The system of equations (2.3), (2.6) is subjected to the initial conditions

$$h = 1 + \mathrm{S}\exp[-x^2/2 - y^2/2], \tag{7.1a}$$

$$h^0 = \mathrm{S}\exp[-x^2/2 - y^2/2], \tag{7.1b}$$

where $\mathrm{S} = 10^{-2}$.

The non-linear simulations are performed using the finite-element software COMSOL Multiphysics. The flow equations are solved in a rectangular domain with periodic boundary conditions, for the variables (h, κ, h^0) using third-order finite elements; the time-marching is obtained by a second-order backward differentiation formula. We consider a domain of size $L_x = 310$ and $L_y = 180$ with periodic boundary conditions and largest mesh element of characteristic size l_c^* in the region, leading to a mesh of approximately 56000 elements. A preliminary analysis shows that the numerical convergence is already achieved with this characteristic size of the elements.

In fig. 15 we show the results at three different times, for the fluid and substrate thickness. As a comparison, on the bottom, the results for $h = 1 + \mathrm{S}\eta$ of the linear simulation of Section 5.2 are reported. The non-linear patterns are very similar to the corresponding linear ones, even if some differences can be highlighted. As time increases, the fluid film increases and the perturbation spreads in concentric circles from the maximum thickness location. Streamwise structures are selected in the downstream part of the response close to the maximum value position, while in the linear simulation the pattern is isotropic in this region. The dominance of streamwise structures in the downstream part is enhanced as u increases (fig. 16).

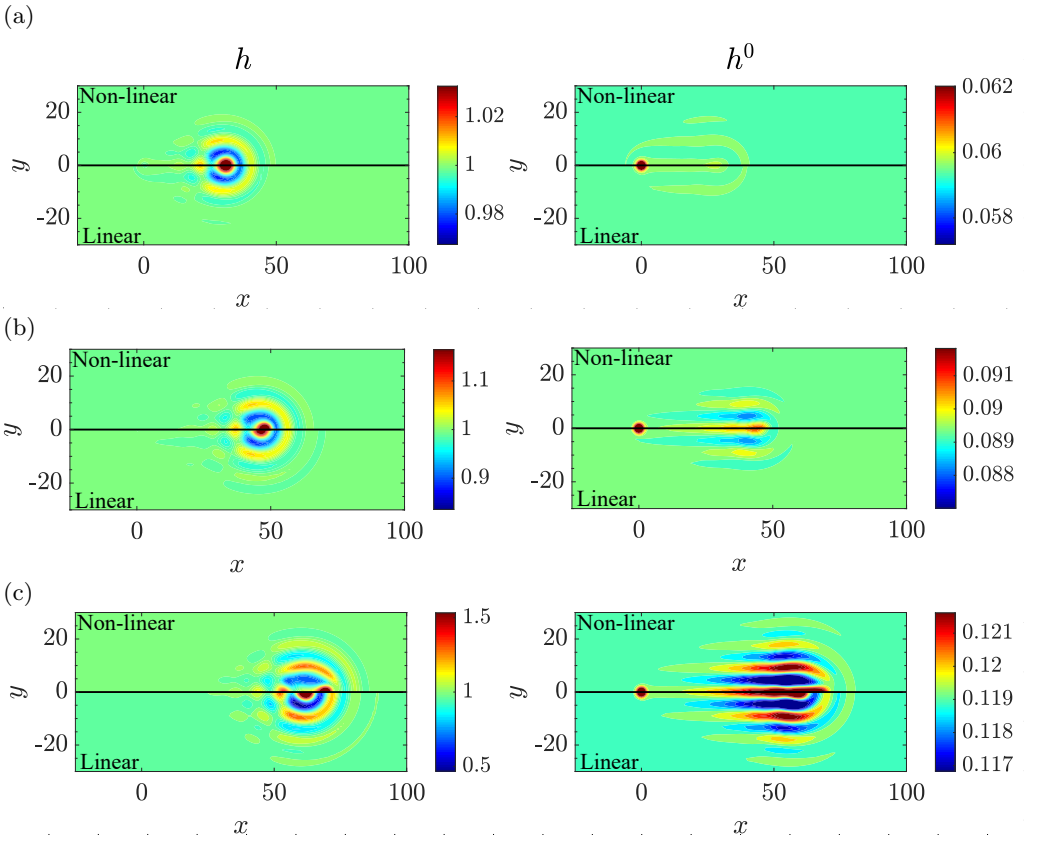

FIGURE 15. Non-linear impulse response of equations (2.3) and (2.6) for $u = 0.77$ and $C = 10^{-3}$, at (a) $t = 40$, (b) $t = 60$, (c) $t = 80$. On the left: fluid thickness response. On the right: substrate thickness response. The colobars are centered around the values $h = 1$ and $h^0 = \check{C}t$.

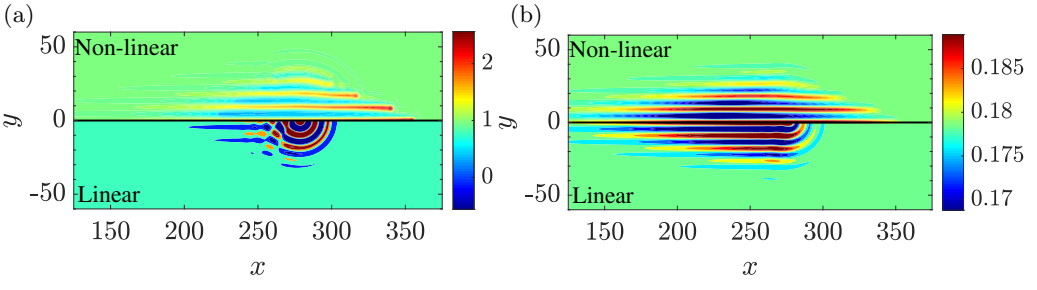

FIGURE 16. Non-linear impulse response of equations (2.3) and (2.6) for $u = 2.31$ and $C = 10^{-3}$, at $t = 120$. (a) fluid thickness response. (b) substrate thickness response. The colobars are centered around the values $h = 1$ and $h^0 = \check{C}t$.

The upstream part shows the same intricate pattern observed in the linear simulations. The substrate thickness presents a defect at the origin, which slowly grows in time. Downstream of the defect at the origin, growing streamwise structures on the substrate emerge and propagate in the domain, with a front well described by a constant angle.

Under the light of the results of the previous linear analyses, we are able now to distinguish the different physical mechanisms underlying the selection of streamwise structures. The selection of streamwise structures both in the fluid film and on the

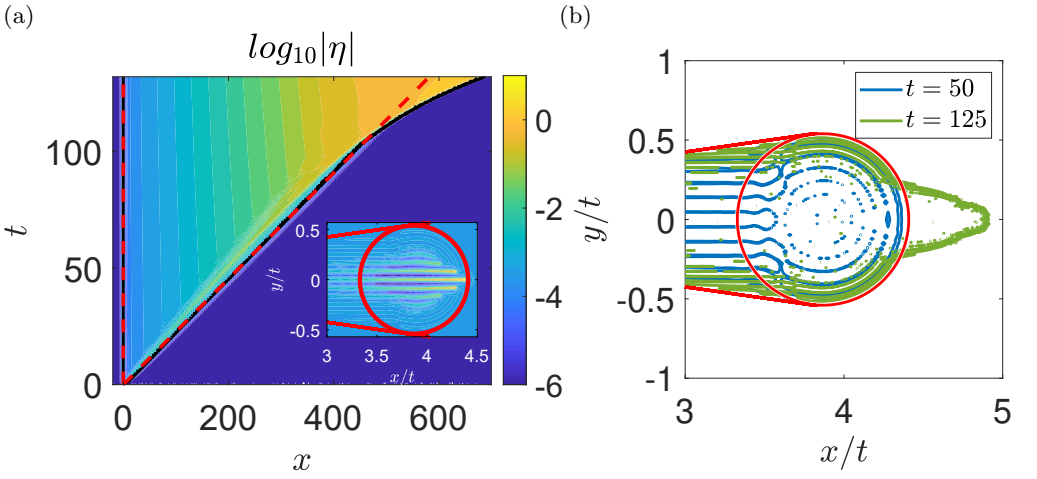

FIGURE 17. (a) Iso-levels of $|\eta|$ as a function of x and t, for $y = 0$. The red dashed lines denote the linear front, while the black line the iso-level that well approximates the front at small times. In the inset: thickness profile for $t = 108$. (b) Iso-level of $|\eta|$ approximating the non-linear front, for $t = 50$ (blue line) and $t = 125$ (green line). The red circle denotes the linear front given by the response in the absence of substrate variations, and the red lines the front given by the steady defect analysis. $u = 3.85$ and $C = 10^{-3}$.

substrate in the downstream part of the initial impulse location is due to the steady defect mechanism of Section 6.2, while in the region upstream the maximum thickness draperies are purely selected by the deposition law. Besides, rivulets emerge also in the downstream part of the wavepacket. This selection is absent in the linearized dynamics and is due to non-linear effects (Ledda *et al.* 2020). The downstream part of the wavepacket is progressively invaded by rivulets with time, thus enhancing the deposition of streamwise structures on the substrate. Thanks to the linear analyses, we conclude that the linear effects are predominant in the upstream part of the wavepacket such that, after all, the selection of streamwise structures occurs for all the values of the linear advection velocity. The deposition of streamwise structures in the downstream part is largely dictated by the non-linear selection of rivulets in the fluid film, whose dominance is enhanced with u.

In fig. 16, we observe that the visible perturbation in the non-linear simulation spreads in a larger region compared to the linear simulation. This implies that the linear front given by the iso-level $\sigma = 0$ changes in the non-linear regime. We thus focus on the structure of the non-linear front with time. The analysis performed with the post-process algorithm could be in principle applied to the results of the non-linear simulations. However, non-linearities generate large wavelengths, altering the band structure of the spectrum of the perturbation observed in the linear simulations. As a consequence, it is no more possible to recover the envelope of the response (Melville 1983; Delbende & Chomaz 1998).

Despite this, following Delbende & Chomaz (1998), it is possible to obtain information about the front by following the iso-levels of the absolute value of the response $|\eta|$. We consider the centerline profile (i.e. $y/t = 0$) and we extend the linear fronts (red dashed lines) in the non-linear regime by following the corresponding iso-level of $|\eta|$ (fig. 17(a)). We assume that this iso-level is a good approximation of the non-linear front. The non-linear front follows the linear one until $t \approx 108$, beyond which it bends and the perturbation spreads in a larger region. In the inset, we report the corresponding

thickness profile at $t = 108$. The maximum thickness location is very close to the linear front. The variation of the iso-level of $|\eta|$ well approximating the non-linear front is reported in fig. 17(b) as a function of $(x/t, y/t)$, for $t = 50$ and $t = 125$. The iso-level well approximates the linear prediction, and at $t = 125$ we observe that the non-linear front has spread downstream in a larger region.

The analysis of the non-linear front shows that, at large times, the perturbation spreads in a larger region than the one predicted by the linear theory. While in the linear regime the advection of perturbation is given by u, in the non-linear regime it is equal to uh^2 (Babchin *et al.* 1983). As the perturbation grows, regions with thickness $h > 1$ travel faster than the flat film and vice versa. Thus, for large enough times, the linear front is eventually reached (downstream for $h > 1$, upstream for $h < 1$). Our case corresponds to (c,d) in fig. 3 of Delbende & Chomaz (1998). For the sake of completeness, we report in Appendix D the results of the non-linear front in the absence of substrate variations. In conclusion, the non-linearities tend to favour streamwise structures and to deform the front in which the perturbation spreads due to the differences in advection.

8. Conclusions and discussion

In this work, we studied the pattern formation of a thin film flowing under an inclined plane, in the presence of material deposition on the substrate, reminiscent of the karst structure formation in limestone caves. We tackled the problem theoretically and numerically studying the linearized dynamics when substrate variations are considered.

The spatio-temporal analysis in the presence of the deposition process was studied in the context of numerical simulations and a novel approach to retrieve the wavepacket properties. The numerical study of the impulse response was generalized to the two-dimensional case with the introduction of the monogenic signal, the two-dimensional analytic continuation of a real signal, based on the Riesz transform. The monogenic signal allows us to reconstruct the amplitude and the phase of the numerical response, and then the asymptotic properties of the wavepacket. This approach, which constitutes the generalization to two propagation directions of the approach introduced in Brancher & Chomaz (1997) and Delbende *et al.* (1998), can be generally used in flows where the dispersion is not known analytically or when the saddle-point tracking becomes too challenging. Besides, this procedure allows one to proceed to an a posteriori description of the response, without the necessity to a priori define the unstable branches of the dispersion relation, making it suitable for the analysis of complex fluid responses. The numerical procedure aims at deriving the asymptotic behavior for $t \to \infty$ using numerical simulations at finite times, and assumes that the amplitude and the phase of the signal subject to the Riesz transform can be separated (i.e. a separation of scales between the variations of the envelope and the oscillations subsists). We verified the validity of the assumptions in the present case by a comparison with the analytical solution in the absence of substrate variations.

We therefore focused on the study of the linear impulse response in the presence of a deposition law. The temporal analysis of the dispersion relation showed only a slight anisotropy which promotes streamwise aligned structures. Motivated by this, we therefore studied the linear impulse response exploiting the post-processing algorithm. We identified (I) an isotropic region that is advected away (fig. 18(a)) and (III) a quasi-steady region propagating downstream (fig. 18(b)) with a front defined by an approximately constant angle, related to the presence of a growing substrate defect at the initial impulse location.

The analysis of the substrate thickness showed that the deposition law selects predomi-

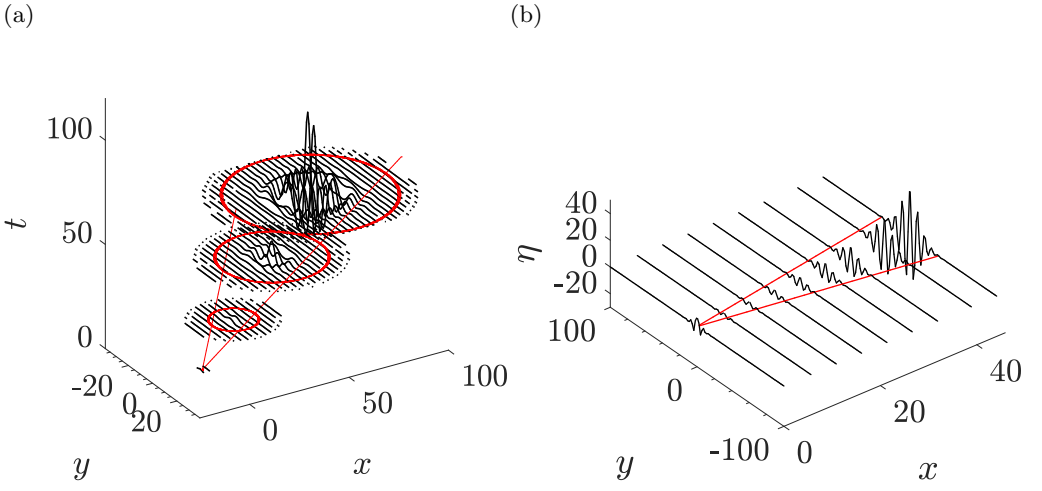

FIGURE 18. Analytical (a) spatio-temporal response to a localized initial perturbation (Section 3.2) and (b) spatial response to a localized steady defect (Section 6.2), in the absence of the deposition process. The red lines denote the limits in which the perturbation spreads.

nant streamwise structures as the wavepacket is advected away, in (II) the upstream part of the traveling wavepacket. Physically, we related this phenomenon to the fact that, in opposition to rivulets, waves are traveling structures. Perturbations are oscillating at fixed locations, thus having a much smaller effect on the substrate topography.

We thus analysed the response to a steady defect, for the pure hydrodynamic problem. The region just downstream of the steady obstacle coincides with the quasi-steady region (III) identified in the deposition case, and it is in good agreement with the analytical Green function for a steady defect (fig. 18(b)). The emergent pattern is characterized by streamwise structures both in the fluid film and on the substrate thickness.

In the non-linear simulations, we exploited the results of the linear analyses and we distinguished the selection mechanisms due to the substrate variations from the non-linear mechanism of rivulets selection in the absence of substrate variations. While in the first case the dominance of streamwise structures is independent of the linear advection velocity, the latter plays a crucial role in the non-linear selection mechanism. The latter promotes the selection of rivulets (in the fluid film) in the downstream part of the traveling wavepacket (I), thus enhancing the deposition of draperies structures. We analyzed the evolution of the fronts between which the perturbation spreads, concluding that the emergence of rivulets modifies the downstream front by nonlinearly increasing the leading edge front velocity.

We conclude that the different selection mechanisms are dominant in different regions of the response. The deposition process couples the hydrodynamic mechanisms of the unsteady response in the absence of substrate variations and the steady response in the presence of localized substrate variations. In common natural environments, the relative importance of the mechanisms may depend on the fluid film and substrate conditions, but always giving rise to predominant draperies structures. The immense diversity of limestone patterns observed in nature may result from secondary instabilities of these predominantly selected primary streamwise-oriented structures.

Acknowledgements

We acknowledge the Swiss National Science Foundation under grant 200021_178971.

Declaration of interests

The authors declare no conflict of interest.

Appendix A. Numerical method and validation

In this section, we introduce the numerical method to solve equations 2.8 in a rectangular domain, with periodic boundary conditions. We consider the Fourier transforms of the functions (η, η^0):

$$\left[\hat{\eta}, \hat{\eta}^0\right]^T = \iint \left[\eta, \eta^0\right]^T e^{-\mathrm{i}\mathbf{k}\cdot\mathbf{x}} \mathrm{d}\mathbf{x}, \tag{A 1}$$

where $\mathbf{k} = (k_x, k_y)$, are respectively the streamwise and spanwise wavenumbers. Applying the Fourier transform to eq. (2.8), the following complex ODE's system is obtained:

$$\frac{d\hat{\eta}}{\mathrm{d}t} = \hat{\eta}(-\mathrm{i}uk_x) + (\hat{\eta} + \hat{\eta}^0)\frac{1}{3}\left(\chi k^2 - k^4\right), \tag{A 2}$$

$$\frac{d\hat{\eta}^0}{\mathrm{d}t} = \check{C}\hat{\eta}, \tag{A 3}$$

where $k = |\mathbf{k}|$. Introducing the vector $\hat{\boldsymbol{\eta}} = [\hat{\eta}, \hat{\eta}^0]^T$, the system of equations reads:

$$\frac{d\hat{\boldsymbol{\eta}}}{\mathrm{d}t} = \begin{bmatrix} \frac{1}{3}\left(\chi k^2 - k^4\right) - \mathrm{i}uk_x & \frac{1}{3}\left(\chi k^2 - k^4\right) \\ \check{C} & 0 \end{bmatrix} \hat{\boldsymbol{\eta}} = A\hat{\boldsymbol{\eta}} \tag{A 4}$$

With the decomposition $\hat{\boldsymbol{\eta}} = \hat{\boldsymbol{\eta}}_r + \mathrm{i}\hat{\boldsymbol{\eta}}_i$, the final system of real ODE's reads:

$$\frac{d\hat{\boldsymbol{y}}}{\mathrm{d}t} = \begin{bmatrix} \frac{d\hat{\boldsymbol{\eta}}_r}{\mathrm{d}t} \\ \frac{d\hat{\boldsymbol{\eta}}_i}{\mathrm{d}t} \end{bmatrix} = \begin{bmatrix} A_r & -A_i \\ A_i & A_r \end{bmatrix} \begin{bmatrix} \hat{\boldsymbol{\eta}}_r \\ \hat{\boldsymbol{\eta}}_i \end{bmatrix} = B\hat{\boldsymbol{y}} \tag{A 5}$$

The solution of this problem can be written as:

$$\hat{\boldsymbol{y}} = \mathrm{expm}[Bt]\hat{\boldsymbol{y}}(0), \tag{A 6}$$

where expm stands for the exponential matrix.

The numerical procedure is implemented in MATLAB. A rectangular domain of size 1000×1000 is considered, with a number of collocation points $N_x = N_y = 1001$. A convergence analysis on (N_x, N_y) has been performed, concluding that convergence is already achieved for 1001 collocation points. No significant changes have been observed increasing the domain size. The initial condition is transformed in the two-dimensional Fourier space using the built-in function for the Fast Fourier Transform *fft2*. Subsequently, the linear system of ODE's is solved using the built-in function for the exponential matrix, and the solution in the space domain is obtained through the Inverse Fast Fourier Transform *ifft2*.

The numerical code is validated against a benchmark case present in the literature for the experimental response in the presence of a steady defect for a thin film flowing over an inclined plane, i.e. $\chi = -1$ and $C = 0$. The initial condition is given by $\eta(x, y, 0) = 0$, and $\eta^0(x, y, 0) = -\exp[-(x^2 + y^2)/2\varsigma^2]$, with $\varsigma = 0.17$, which gives the same integral value of the experimental step-down defect used in Decré & Baret (2003) and does not vary with time. In the inertialess case and absence of defects, the flow over an inclined plane is stable and the solution is a film of constant thickness (Kalliadasis *et al.* 2011). The presence of a localized steady defect creates a region close to the depression characterized by a variation of the free surface elevation $\eta + \eta^0$ (see fig. 19(a)). In the region just upstream of

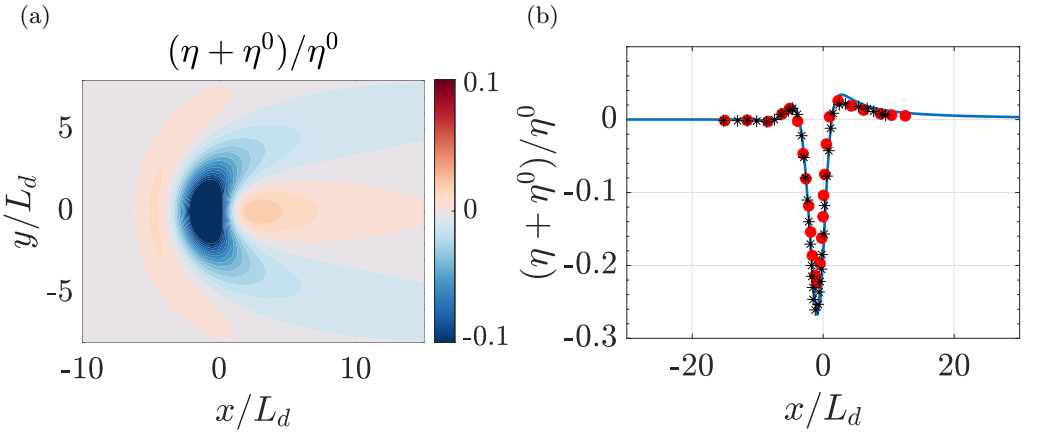

FIGURE 19. Two-dimensional linear response in the presence of a localized steady defect for the flow over an inclined planar substrate, at $y = 0$ as a function of the streamwise coordinate, for $u = 16.75$. Results are rescaled using the adimensionalization reported in Decré & Baret (2003) ($L_d = (\gamma h_N/3\rho g cos(\theta))^{1/3}$). (a) Response in the (x, y) plane. (b) Comparison between the experimental (red dots) and numerical (black stars) results of Decré & Baret (2003) and the numerical solution (blue line).

the depression, there is a small increase in the free surface elevation, followed by a strong decrease. Downstream, there is an overshoot greater than the initial thickness followed by a recovery of the flat film conditions. In fig. 19(b) we show a comparison of the results of our model with the experimental and theoretical results of Decré & Baret (2003), for the free surface elevation at $y = 0$. Results are rescaled using their adimensionalization. The comparison shows a good agreement, thus validating the numerical procedure.

Appendix B. Evaluation of the imaginary part of the spatial wavenumbers from the spatio-temporal growth rate

In this Appendix, we demonstrate eq. (4.15,4.16) by generalizing to the two-dimensional case the approach outlined in Delbende *et al.* (1998). We consider:

$$\omega''(v_x, v_y) = \omega - k_x v_x - k_y v_y. \tag{B 1}$$

We derive eq. (B 1) with respect to the group velocity v_x along the x direction:

$$\frac{\partial \omega''}{\partial v_x} = \frac{\partial \omega}{\partial v_x} - \frac{\partial k_x}{\partial v_x} v_x - k_x - \frac{\partial k_y}{\partial v_x} v_y. \tag{B 2}$$

Since $\omega = \omega(k_x, k_y)$, we evaluate the derivative as follows:

$$\frac{\partial[\omega(k_x, k_y)]}{\partial v_x} = \underbrace{\frac{\partial \omega}{\partial k_x}}_{v_x} \frac{\partial k_x}{\partial v_x} + \underbrace{\frac{\partial \omega}{\partial k_y}}_{v_y} \frac{\partial k_y}{\partial v_x}, \tag{B 3}$$

being v_x and v_y real (Delbende *et al.* 1998). Substituting in eq. (B 2), the imaginary part of the streamwise wavenumber is obtained:

$$\mathrm{Im}(k_x) = -\frac{\partial \sigma}{\partial v_x}. \tag{B 4}$$

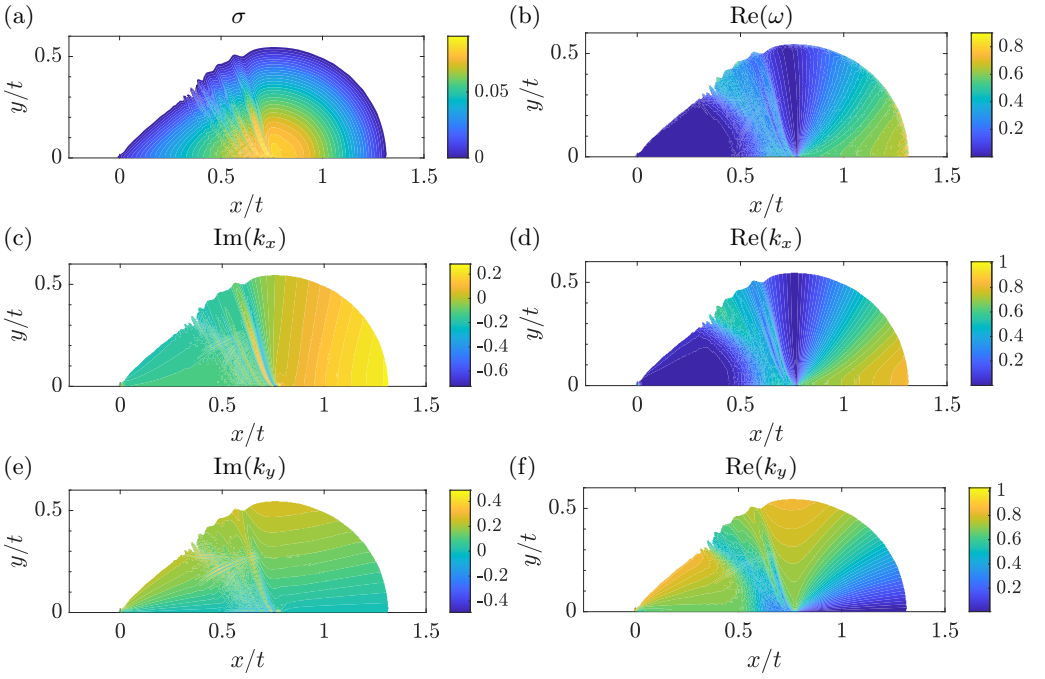

FIGURE 20. Asymptotic properties from the post process algorithm (Section 4), for $u = 0.77$ and $C = 10^{-3}$. (a) spatio-temporal growth rate. (b) Real part of the complex frequency. (c) Imaginary part of the streamwise wavenumber. (d) Real part of the streamwise wavenumber. (e) Imaginary part of the spanwise wavenumber. (f) Real part of the spanwise wavenumber.

Deriving ω'' with respect to v_y and following the same procedure, Im(k_y) reads:

$$\mathrm{Im}\,(k_y) = -\frac{\partial \sigma}{\partial v_y}. \tag{B 5}$$

Appendix C. Results of the post-processing algorithm for $C = 10^{-3}$

In this section, for the sake of completeness, we report the results of the post-processing algorithm of Section 4 applied for the case in the presence of the deposition process (Section 5.3), for $C = 10^{-3}$. The results are similar to those observed in the case $C = 10^{-5}$ (fig. 8), with a front downstream of the initial position more curved and the region where the two contributions (quasi-steady and spatio-temporal) interact displaced downstream.

Appendix D. Non-linear front in the absence of substrate variations

In this Section, we report the results of the evaluation of the non-linear front for the case in the absence of substrate variations, for $u = 3.85$. The results show a deformation of the front similar to fig. 17, without the quasi-steady part propagating downstream.

REFERENCES

ARRATIA, C.L, MOWLAVI, S. & GALLAIRE, F. 2018 Absolute/convective secondary instabilities and the role of confinement in free shear layers. *Physical Review Fluids* **3** (5), 053901.

BABCHIN, A.J., FRENKEL, A.L., LEVICH, B.G. & SIVASHINSKY, G.I. 1983 Nonlinear saturation of Rayleigh–Taylor instability in thin films. *The Physics of fluids* **26** (11), 3159–3161.

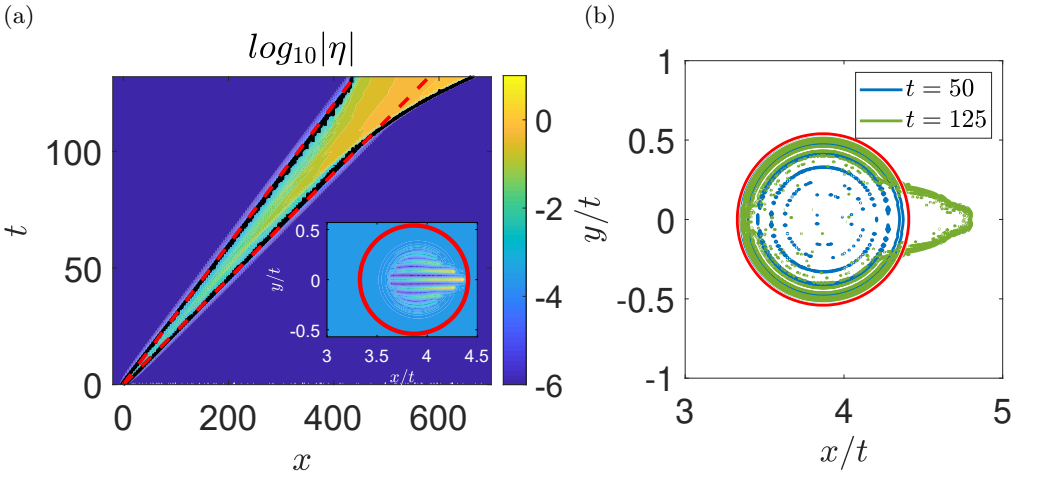

FIGURE 21. $u = 3.85$, no substrate variations. (a) Iso-levels of $|\eta|$ as a function of x and t, for $y = 0$. The read dashed lines denote the linear front, while the black line the iso-level that well approximates the front at small times. In the inset: thickness profile for $t = 108$. (b) Iso-level of $|\eta|$ approximating the non-linear front, for $t = 50$ (blue line) and $t = 125$ (green line). The red line denotes the linear front in absence of substrate variations.

BARLOW, N.S., HELENBROOK, B.T. & WEINSTEIN, S.J. 2017 Algorithm for spatio-temporal analysis of the signalling problem. *IMA Journal of Applied Mathematics* **82** (1), 1–32.

BERS, A. 1975 Linear waves and instabilities. In *Plasma physics–les houches 1972*.

BERTAGNI, M. B. & CAMPOREALE, C. 2017 Nonlinear and subharmonic stability analysis in film-driven morphological patterns. *Physical Review E* **96** (5), 053115.

BRANCHER, P. & CHOMAZ, J-M 1997 Absolute and convective secondary instabilities in spatially periodic shear flows. *Physical review letters* **78** (4), 658.

BREVDO, L. 1991 Three-dimensional absolute and convective instabilities, and spatially amplifying waves in parallel shear flows. *Zeitschrift für angewandte Mathematik und Physik ZAMP* **42** (6), 911–942.

BRIGGS, R. J. 1964 Electron stream interaction with plasmas. In *Handbook of Plasma Physics*. MIT Press.

BRUN, P-T, DAMIANO, A., RIEU, P., BALESTRA, G. & GALLAIRE, F. 2015 Rayleigh-Taylor instability under an inclined plane. *Physics of Fluids* **27** (8), 084107.

BUHMANN, D. & DREYBRODT, W. 1985 The kinetics of calcite dissolution and precipitation in geologically relevant situations of karst areas: 1. open system. *Chemical geology* **48** (1-4), 189–211.

BULOW, T. & SOMMER, G. 2001 Hypercomplex signals-a novel extension of the analytic signal to the multidimensional case. *IEEE Transactions on signal processing* **49** (11), 2844–2852.

CAMPOREALE, C. 2015 Hydrodynamically locked morphogenesis in karst and ice flutings. *Journal of Fluid Mechanics* **778**, 89–119.

CAMPOREALE, C. & RIDOLFI, L. 2012 Hydrodynamic-driven stability analysis of morphological patterns on stalactites and implications for cave paleoflow reconstructions. *Phys. Rev. Lett.* **108**, 238501.

CARRIERE, P. & MONKEWITZ, P.A. 1999 Convective versus absolute instability in mixed rayleigh–bénard–poiseuille convection. *Journal of Fluid Mechanics* **384**, 243–262.

CHAROGIANNIS, A., DENNER, F., VAN WACHEM, B. G. M., KALLIADASIS, S., SCHEID, B. & MARKIDES, C. N. 2018 Experimental investigations of liquid falling films flowing under an inclined planar substrate. *Physical Review Fluids* **3** (11), 114002.

COHEN, C., BERHANU, M., DERR, J. & COURRECH DU PONT, S. 2016 Erosion patterns on dissolving and melting bodies. *Phys. Rev. Fluids* **1**, 050508.

D'ALESSIO, S.J.D., PASCAL, J.P., JASMINE, H.A. & OGDEN, K.A. 2010 Film flow over heated wavy inclined surfaces. *Journal of Fluid Mechanics* **665**, 418–456.

Decré, M. M. J. & Baret, J.-C. 2003 Gravity-driven flows of viscous liquids over two-dimensional topographies. *Journal of Fluid Mechanics* **487**, 147–166.

Delbende, I. & Chomaz, J-M 1998 Nonlinear convective/absolute instabilities in parallel two-dimensional wakes. *Physics of Fluids* **10** (11), 2724–2736, arXiv: https://doi.org/10.1063/1.869796.

Delbende, I., Chomaz, J-M & Huerre, P. 1998 Absolute/convective instabilities in the batchelor vortex: a numerical study of the linear impulse response. *Journal of Fluid Mechanics* **355**, 229–254.

Felsberg, M. & Sommer, G. 2001 The monogenic signal. *IEEE transactions on signal processing* **49** (12), 3136–3144.

Fermigier, M., Limat, L., Wesfreid, J.E., Boudinet, P. & Quilliet, C. 1992 Two-dimensional patterns in rayleigh-taylor instability of a thin layer. *Journal of Fluid Mechanics* **236**, 349–383.

Gallaire, F. & Chomaz, J-M 2003 Mode selection in swirling jet experiments: a linear stability analysis. *Journal of Fluid Mechanics* **494**, 223–253.

Hahn, S.L. 2003 Complex signals with single-orthant spectra as boundary distributions of multidimensional analytic functions. *Bull. Pol. Ac.: Tech* **2** (2), 155–161.

Hayes, M., O'Brien, S. B. G. & Lammers, J. H. 2000 Green's function for steady flow over a small two-dimensional topography. *Physics of Fluids* **12** (11), 2845–2858, arXiv: https://aip.scitation.org/doi/pdf/10.1063/1.1311970.

Heining, C & Aksel, N 2009 Bottom reconstruction in thin-film flow over topography: Steady solution and linear stability. *Physics of Fluids* **21** (8), 083605.

Hill, C.A., Forti, P. & Shaw, T.R. 1997 *Cave minerals of the world*, , vol. 238. National speleological society Huntsville.

Huerre, P. & Monkewitz, P. A. 1990 Local and global instabilities in spatially developing flows. *Annual Review of Fluid Mechanics* **22** (1), 473–537.

Juniper, M. P. 2007 The full impulse response of two-dimensional jet/wake flows and implications for confinement. *Journal of Fluid Mechanics* **590**, 163–185.

Kalliadasis, S., Bielarz, C. & Homsy, G.M. 2000 Steady free-surface thin film flows over topography. *Physics of Fluids* **12** (8), 1889–1898.

Kalliadasis, S., Ruyer-Quil, C., Scheid, B., Velarde, M.G. & García, M. 2011 *Falling liquid films*, , vol. 176. Springer Science & Business Media.

Kofman, N., Rohlfs, W., Gallaire, F., Scheid, B. & Ruyer-Quil, C. 2018 Prediction of two-dimensional dripping onset of a liquid film under an inclined plane. *International Journal of Multiphase Flow* **104**, 286–293.

Ledda, P.G., Lerisson, G., Balestra, G. & Gallaire, F. 2020 Instability of a thin viscous film flowing under an inclined substrate: the emergence and stability of rivulets. *Journal of Fluid Mechanics* **904**, A23.

Lerisson, G. 2017 Stabilité d'une onde de gravité interne, analyse locale, globale et croissance transitoire. PhD thesis, thèse de doctorat dirigée par Chomaz, Jean-Marc et Ortiz Clerc, Sabine Mécanique des fluides Paris Saclay 2017.

Lerisson, G., Ledda, P.G., Balestra, G. & Gallaire, F. 2019 Dripping down the rivulet. *Phys. Rev. Fluids* **4**, 100504.

Lerisson, G., Ledda, P.G., Balestra, G. & Gallaire, F. 2020 Instability of a thin viscous film flowing under an inclined substrate: steady patterns. *Journal of Fluid Mechanics* **898**, A6.

Lister, J.R., Rallison, J.M. & Rees, S.J. 2010 The nonlinear dynamics of pendent drops on a thin film coating the underside of a ceiling. *Journal of Fluid Mechanics* **647**, 239–264.

Marthelot, J., Strong, E. F., Reis, P. M. & Brun, P-T. 2018 Designing soft materials with interfacial instabilities in liquid films. *Nature communications* **9** (1), 4477.

Meakin, P. & Jamtveit, B. 2010 Geological pattern formation by growth and dissolution in aqueous systems. *Proceedings of the Royal Society A: Mathematical, Physical and Engineering Sciences* **466** (2115), 659–694.

Melville, W.K. 1983 Wave modulation and breakdown. *Journal of Fluid Mechanics* **128**, 489–506.

Mowlavi, S., Arratia, C. & Gallaire, F. 2016 Spatio-temporal stability of the kármán vortex street and the effect of confinement. *Journal of Fluid Mechanics* **795**, 187–209.

Rayleigh 1882 Investigation of the character of the equilibrium of an incompressible heavy fluid of variable density. *Proceedings of the London Mathematical Society* **s1-14** (1), 170–177.

Scheid, B., Kofman, N. & Rohlfs, W. 2016 Critical inclination for absolute/convective instability transition in inverted falling films. *Physics of Fluids* **28** (4), 044107.

Short, M.B., Baygents, J.C., Beck, J.W., Stone, D.A., Toomey, R.S. & Goldstein, R.E. 2005*a* Stalactite growth as a free-boundary problem: A geometric law and its platonic ideal. *Phys. Rev. Lett.* **94**, 018501.

Short, M.B, Baygents, J.C & Goldstein, R.E. 2005*b* Stalactite growth as a free-boundary problem. *Physics of fluids* **17** (8), 083101.

Stein, E.M. & Weiss, G. 2016 *Introduction to Fourier analysis on Euclidean spaces*, , vol. 32. Princeton university press.

Taylor, G. I. 1950 The instability of liquid surfaces when accelerated in a direction perpendicular to their planes. i. *Proceedings of the Royal Society of London. Series A. Mathematical and Physical Sciences* **201** (1065), 192–196.

Trefethen, L.N. & Bau III, D. 1997 *Numerical linear algebra*, , vol. 50. Siam.

Tseluiko, D, Blyth, MG & Papageorgiou, DT 2013 Stability of film flow over inclined topography based on a long-wave nonlinear model. *Journal of Fluid Mechanics* **729**, 638–671.

Unser, M., Sage, D. & Van De Ville, D. 2009 Multiresolution monogenic signal analysis using the riesz–laplace wavelet transform. *IEEE Transactions on Image Processing* **18** (11), 2402–2418.

Van Saarloos, W. 2003 Front propagation into unstable states. *Physics reports* **386** (2-6), 29–222.

Vesipa, R, Camporeale, C & Ridolfi, L 2015 Thin-film-induced morphological instabilities over calcite surfaces. *Proceedings of the Royal Society A: Mathematical, Physical and Engineering Sciences* **471** (2176), 20150031.

Weinstein, S.J. & Ruschak, K.J. 2004 Coating flows. *Annu. Rev. Fluid Mech.* **36**, 29–53.

Wilson, S.D.R. 1982 The drag-out problem in film coating theory. *Journal of Engineering Mathematics* **16** (3), 209–221.